

Creep burst coincident with faulting in marble observed in 4D synchrotron X-ray imaging triaxial compression experiments

Jessica McBeck^{1,1}, François Renard^{1,1}, Neelima Kandula^{1,1}, and Benoit Jérôme Bertrand Cordonnier^{2,2}

¹University of Oslo

²ETH Zürich

November 30, 2022

Abstract

Faults in carbonate rocks show both seismic and aseismic deformation processes, leading to a wide range of slip velocities. We deformed two centimeter-scale cores of Carrara marble at 25°C, under in-situ conditions of stress of 2-3 km depth, and imaged the nucleation and growth of creeping faults using dynamic synchrotron X-ray microtomography with micrometer spatial resolution. The first sample was under a constant confinement of 30 MPa and no pore fluid. The second sample was under a confinement in the range 35-23 MPa, with 10 MPa pore fluid pressure. We increased the axial stress by steps until creep deformation occurred and imaged deformation in 4D during creep. The samples deformed with a steady-state strain rate when the differential stress was constant, a process called creep. However, for both samples, we also observed transient events that include the acceleration of creep, i.e., creep bursts, phenomena similar to slow slip events that occur in continental active faults. During these transient creep events, strain rates increase and correlate in time with strain localization and the development of system-spanning fault networks. In both samples, the acceleration of opening and shearing of microfractures accommodated creep bursts. Using high-resolution time-lapse X-ray micro-tomography imaging, and digital image correlation, during triaxial deformation allowed quantifying creep in laboratory faults at sub-grain spatial resolution, and demonstrates that transient creep events (creep bursts) correlate with the nucleation and growth of faults.

1 **Creep burst coincident with faulting in marble observed in 4D synchrotron X-ray**
2 **imaging triaxial compression experiments**

3
4 **François Renard^{1,2}, Neelima Kandula¹, Jessica McBeck¹, Benoît Cordonnier¹**

5 ¹ Physics of Geological Processes, The Njord Centre, Department of Geosciences, University of
6 Oslo, Oslo, Norway

7 ² University Grenoble Alpes, University Savoie Mont Blanc, CNRS, IRD, IFSTTAR, ISTerre,
8 38000 Grenoble, France

9
10 Corresponding author: François Renard (francois.renard@geo.uio.no)

11
12 **Key Points:**

- 13 • Transient creep bursts under constant stress conditions are detected in laboratory
14 experiments
- 15 • The bursts correlate with an increase of dilatancy, including the opening and rotation of
16 microfractures
- 17 • The macroscopically-detected bursts correlate with the microscopically-observed
18 nucleation, growth, dilation and shearing of faults
19

20 **Abstract**

21 Faults in carbonate rocks show both seismic and aseismic deformation processes, leading to a
22 wide range of slip velocities. We deformed two centimeter-scale cores of Carrara marble at
23 25°C, under in-situ conditions of stress of 2-3 km depth, and imaged the nucleation and growth
24 of creeping faults using dynamic synchrotron X-ray microtomography with micrometer spatial
25 resolution. The first sample was under a constant confinement of 30 MPa and no pore fluid. The
26 second sample was under a confinement in the range 35-23 MPa, with 10 MPa pore fluid
27 pressure. We increased the axial stress by steps until creep deformation occurred and imaged
28 deformation in 4D during creep. The samples deformed with a steady-state strain rate when the
29 differential stress was constant, a process called creep. However, for both samples, we also
30 observed transient events that include the acceleration of creep, i.e., creep bursts, phenomena
31 similar to slow slip events that occur in continental active faults. During these transient creep
32 events, strain rates increase and correlate in time with strain localization and the development of
33 system-spanning fault networks. In both samples, the acceleration of opening and shearing of
34 microfractures accommodated creep bursts. Using high-resolution time-lapse X-ray micro-
35 tomography imaging, and digital image correlation, during triaxial deformation allowed
36 quantifying creep in laboratory faults at sub-grain spatial resolution, and demonstrates that
37 transient creep events (creep bursts) correlate with the nucleation and growth of faults.

38

39 **Plain Language Summary**

40 Active faults may slip at velocities close to one meter per second during earthquakes, but may
41 also slip at much slower rates, in creep. Sometimes such creep is continuous in time, sometimes
42 it is transient and occurs as creep bursts, also called slow slip events. Using state of the art
43 synchrotron X-ray imaging of core samples of Carrara marble, we identified such creep bursts
44 under conditions of pressure and temperature similar to that in the Earth's upper crust. Our 4D
45 imaging technique allows seeing through the sample and characterizing the microphysical
46 processes that produce creep bursts. Results show that acceleration of microfractures nucleation,
47 growth and coalescence in the sample may lead to the formation of system-spanning faults that
48 coincide in time with the macroscopically-observed creep burst. These results demonstrate that
49 creep bursts do not only correspond to slow slip events on active preexisting faults, but may also
50 indicate the development of new active faults.

51

52 **1 Introduction**

53 Fault slip can reach velocities on the order of a meter per second during earthquakes, or
54 much slower velocities when displacements occur over hours to weeks. Events of such slower
55 velocities, known as creep transients, or slow slip events when applied to active faults, indicate a
56 permanent deformation whose rate ranges between the tectonic loading rate and earthquake rates
57 (e.g., Bürgmann, 2018). At least two physical mechanisms have been linked to creep in the
58 Earth's upper crust. Brittle creep can occur by the chemically-activated slow growth and
59 coalescence of microfractures (Scholz, 1968; Brantut et al., 2013). Alternatively, pressure
60 solution creep arises from the coupling between mechanical and chemical forces at the grain
61 scale such that mass transfer through dissolution and precipitation processes controls volumetric
62 deformation (e.g., Rutter, 1976; Gratier et al., 2013). The rheological laws of these two

63 mechanisms describe strain rate as a function of a series of mechanical, chemical and
64 petrophysical parameters, such as stress, temperature, rock composition, grain size and fluid
65 composition.

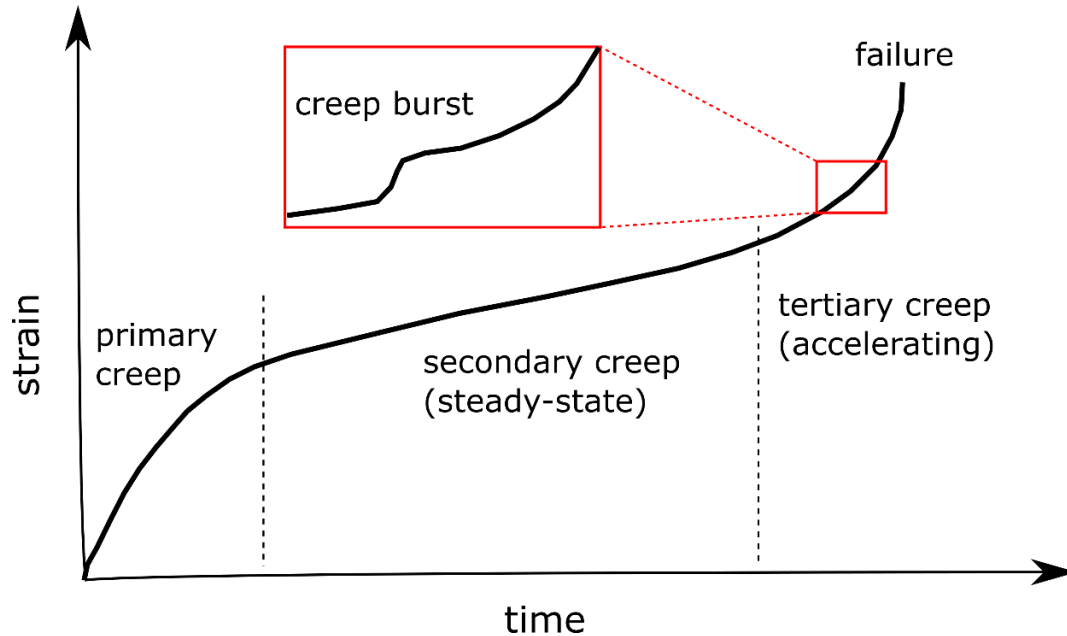
66 When the system is subjected to less than 90% of failure stress, the creep rate is usually
67 constant through time (e.g. Lockner 1993). When approaching failure, the coalescence of
68 microfractures may lead to an exponential or power law increase of creep rate, until catastrophic
69 failure (Reches and Lockner, 1994; Main, 2000; Amitrano and Helmstetter, 2006). In creeping
70 faults, the creep rate may be constant through time, corresponding to steady-state slip. However,
71 transient stages of the acceleration of slow displacements in continental faults have been
72 observed in borehole strain meters (Linde et al., 1996) and in geodetic data (Crescentini et al.,
73 1999; Jolivet et al., 2013). Such creep bursts, or slow slip events, are observed as periods of the
74 increase of slip rate before the fault either becomes locked again or continues to creep at a lower
75 rate. Creep rates measured in major continental faults using time-lapse satellite interferometry
76 indicate that slow slip events can have a wide range of slip surface areas and durations (Jolivet et
77 al., 2015). Some slow slip events can occur on a fault tens of years after a major earthquake
78 (Aslan et al., 2019). Slow slip events can also trigger seismicity (Lohmann and McGuire, 2007)
79 and may control the nucleation process before some major earthquakes (Bouchon et al., 2011).
80 Creep transients induced by anthropogenic fluid injections can also trigger seismicity at the
81 meter to kilometer scales (Guglielmi et al., 2015; Wei et al., 2015).

82 Because creep deformation can precede seismic failure in rocks, an acceleration of creep
83 may indicate an approaching catastrophic event (e.g., Kranz, 1980). This recognition led to the
84 concept of predicting the time to failure of major earthquakes, landslides, and volcanic eruptions
85 (Voigt, 1989; Main, 1999). The creep evolution of some landslides before failure follows this
86 concept (Carlà et al., 2019). However, transient slip acceleration does not always indicate the
87 onset of a catastrophic failure, as for the Mud Creek landslide in California, for example
88 (Handwerger et al., 2019).

89 Observations of rock creep in the crust have motivated the development of laboratory
90 experiments to measure the process and propose rheological laws. Since early creep experiments
91 on sedimentary rocks (Griggs, 1939) and granodiorite and gabbro rocks (Lomnitz, 1953), series
92 of laboratory experiment studies have characterized brittle creep in various rocks, such as granite
93 (Kranz and Scholz, 1977; Lockner and Byerlee, 1977; Ross et al., 1983; Kie et al., 1989;
94 Lockner, 1993; Lei et al., 2000), basalts (Heap et al., 2011), amphibolite (Satoh et al., 1996),
95 marble (Yang et al., 2015; Quintanilla-Terminel and Evans, 2016; Tal et al., 2016; Liu and Shao,
96 2017) and sandstone (Ngwenya et al., 2000; Baud and Meredith, 1997; Tsai et al., 2008; Shengqi
97 and Jiang, 2010). In all of the experiments that reached failure, an acceleration of creep and an
98 increase of acoustic emissions occurred before failure, suggesting the predictability of the time to
99 failure. However, experimental techniques that use acoustic emission recording are blind to
100 aseismic deformation mechanisms at the grain scale because they can only detect the seismic
101 component of deformation. This limitation challenges attempts to estimate the time to failure
102 from microstructural parameters, such as the evolving fracture network geometry, and the
103 validation of theoretical studies on creep in rocks.

104 In creep experiments under constant stress conditions, the macroscopic axial strain rate
105 may increase or decrease, often with three main stages until macroscopic failure (e.g., Lockner,
106 1993). First, primary creep occurs with an initial non-linear increase in strain with time (Figure
107 1). Next, the onset of secondary creep occurs as a decrease in strain rate, producing a quasi-linear

108 relationship between strain and time. Finally, tertiary creep occurs as an acceleration of strain
 109 with an exponential or power law dependence that ends with catastrophic failure (Figure 1). In
 110 the present study, we show in laboratory experiments that the stage of tertiary creep may contain
 111 transient accelerations of strain, i.e., creep bursts, superimposed on the exponential or power law
 112 trend of strain and time.



113
 114 Figure 1: Sketch of the evolution of strain until sample failure during a laboratory creep test,
 115 with three stages: primary, secondary and tertiary creep. The inset shows a transient acceleration
 116 of strain, also called creep burst.

117
 118 A key question in studying creep processes is how mechanisms at the grain scale, such as
 119 microfracturing, interact at mesoscopic and then macroscopic scales to produce the observed
 120 permanent creep or transient creep bursts observed in the upper crust (e.g. Brantut et al., 2013).
 121 The rock deformation experiments in the creep regime with dynamic X-ray microtomography
 122 imaging (4D μ CT), described in the present study, enable linking the macroscale behavior and the
 123 microscale processes under in-situ conditions of the upper crust. This technique allows seeing
 124 within a rock sample while it deforms, with spatial resolution below the grain scale. Here, we
 125 show that the nucleation and growth of microfractures accommodate steady-state creep under
 126 constant stress conditions. A creep burst detected during each experiment coincides in time with
 127 the nucleation and propagation of system-spanning fault networks. We track the microstructural
 128 geometric properties of the microfractures and the local incremental strain deformation with
 129 digital volume correlation. Results allow characterizing the evolution of porosity, dilation,
 130 compaction and shear strain before, during, and after the creep burst event.

131

132 **2 Materials and Methods**

133 2.1 Dynamic synchrotron in-situ experiments

134 The rock samples used here are cylindrical cores, 5 mm in diameter and 10 mm in height,
 135 drilled from a block of Carrara marble. They come from the same block used in the experiments
 136 of rock failure performed in Kandula et al. (2019). Carrara marble is a coarse-grained, nearly
 137 pure calcite rock with grain size in the range of 100-200 micrometers and initial (undeformed)
 138 porosity less than 1%. Each core sample was inserted into a Vitton jacket and between two
 139 stainless steel pistons. The interfaces between the samples and the piston were not lubricated.
 140 This sample assembly was mounted into the Hades triaxial rock deformation apparatus. The
 141 details of the apparatus, including sketch and operating conditions are described in Renard et al.
 142 (2016). This apparatus is installed on the beamline ID19 at the European Synchrotron Radiation
 143 Facility (ESRF) and is used to perform 4D μ CT imaging during rock physics experiments at in-
 144 situ conditions of the upper crust. Table 1 describes the experimental conditions for the two
 145 samples. Figure 2 shows the axial stress, confining pressure, differential stress and axial strain as
 146 a function of time. Experiments were performed at the room temperature of the hutch of
 147 beamline ID19 at ESRF, in the range 23-25 °C.

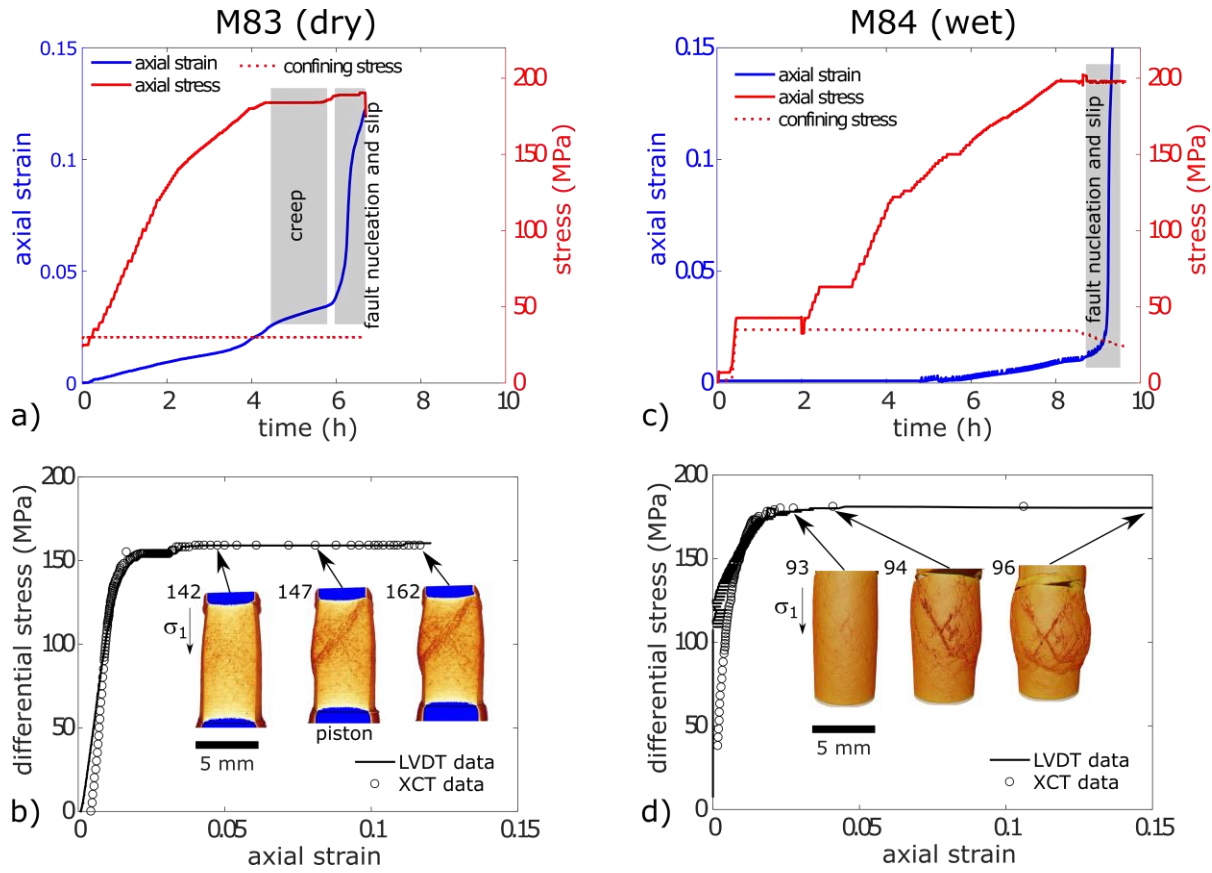
148 The μ CT data were acquired by rotating the Hades rig, with the sample inside, over 180°
 149 and taking either 1800 (sample M83) or 1600 (sample M84) radiographs using the full white
 150 beam of the synchrotron. In these experiments, the Hades rig acts as a filter for X-rays so that an
 151 equivalent energy of 85 keV crosses the sample. Each scan duration was two minutes with
 152 another two minutes between scans. As a result, we acquired μ CT scans every four minutes.
 153 Tomographic reconstruction is performed using the program PyHST2 (Mirone et al., 2014). The
 154 voxel size is $6.5 \mu\text{m}^3$ and the spatial resolution is $6.5 \mu\text{m}$. The tomograms map the three-
 155 dimensional X-ray attenuation in the samples, with the calcite grains having a stronger
 156 attenuation (light gray values) than air-filled voids (dark gray values). Each tomogram of the
 157 rock sample contained around $7.1 \cdot 10^8$ voxels.

158

159 Table 1: Experimental conditions for samples M83 and M84. P_c : confining pressure; P_p : pore
 160 fluid pressure; P_{oring} : differential pressure due to friction in the O-rings of the rig; T: temperature;
 161 σ_f : differential stress at macroscopic failure; ε_y : macroscopic axial strain at yield; nb. XCT:
 162 number of 3D microtomography tomograms acquired during the experiment; duration: total
 163 duration of the experiment from the onset of loading to unloading.

sample	P_c (MPa)	P_p (MPa)	P_{oring} (MPa)	T (°C)	σ_f (MPa)	ε_y	nb. XCT scans	duration (hours)
M83	30	0	10	23	154	0.036	162	6.7
M84	35 → 23	10	2	25	180	0.025	100	9.7

164



165

166 Figure 2: Stress, strain, and X-ray tomography acquisitions for the two samples of Carrara
 167 marble M83 (no pore fluid, left) and M84 (with pore fluid, right). Axial strain, axial stress and
 168 confining stress as a function of time for experiment M83 (a) and M84 (c). The shaded
 169 rectangular areas correspond to periods where the stresses are constant and the sample deforms
 170 either by volumetric creep (i.e. without localization at the sample scale) or through the slow
 171 nucleation and growth of a fault network during a creep burst. b, d) The axial strain is measured
 172 with two independent techniques, with the displacement transducer (LVDT), and from the 3D
 173 tomograms (XCT). Each circle indicates the acquisition of a 3D tomogram. Insets show views of
 174 the sample and fault formation. Numbers indicate the number of the 3D tomogram. For
 175 experiment M83, around twenty tomograms were acquired during fault network nucleation and
 176 formation (i.e. creep burst). For experiment M84, only three tomograms were acquired during
 177 macroscopic fault formation (i.e. creep burst). The largest principle stress, σ_1 , is parallel to the
 178 axis of the cylindrical sample.

179

180 2.2 Stress control and axial strain measurement

181 For both samples, the axial stress, σ_1 , confining pressure, P_c , and pore pressure, P_p , are
 182 controlled by independent pumps connected to the Hades rig. The differential stress in the
 183 sample is $\sigma_{diff} = \sigma_1 - (P_c - P_p) - P_{oring}$, where P_{oring} is pressure caused by the friction of
 184 the O-rings of the rig (Table 1). For the first sample, M83 (dry), the confining pressure was
 185 constant and equal to 30 MPa, with no fluid pressure. The axial stress was increased by steps of 5

186 MPa below a differential stress of 100 MPa, then by steps of 2 MPa between differential stresses
187 of 100 MPa and 120 MPa, then steps of 1 MPa until a differential stress of 154 MPa was
188 reached. The sample was left under a constant differential stress of 154 MPa and then started to
189 creep (left gray rectangle in Figure 2a). A first series of 3D radiographs was then acquired
190 (Figure 3a). Then, the differential stress was increased to 159 MPa, cycled four times between
191 158 and 159 MPa to enhance creep, and left constant at 159 MPa for 100 minutes (right gray
192 rectangle in Figure 2a), during which a fault network propagated across the sample (Figure 3b).
193 This fault propagation corresponds to the creep burst observed macroscopically (Figure 3b).
194 Around twenty tomograms were acquired during this event, between scan numbers 139 and 162
195 (e.g., Figures 2b, 3b).

196 For the second sample, M84 (wet), the initial confining pressure was set to 35 MPa
197 during most of the experiment and then reduced to 23 MPa at the end of the experiment. The
198 fluid pressure was constant and equal to 10 MPa. The axial stress was increased by steps of 5
199 MPa below a differential stress of 93 MPa, then by steps of 2 MPa between differential stresses
200 of 93 MPa and 133 MPa, then steps of 1 MPa until a differential stress of 165 MPa was reached.
201 At this stress level, the axial stress was 200 MPa, the maximum available on the Hades rig. We
202 acquired a series of tomograms, and measured negligible creep of the sample. Because of the
203 limited time available at the ESRF for this experiment, the confining pressure was reduced by
204 steps of 1 MPa to 23 MPa to increase creep rate. At 23 MPa confining stress, corresponding to
205 172 MPa differential stress, several faults nucleated in the sample and propagated within four
206 minutes, resulting in macroscopic failure (gray rectangle in Figure 2c, Figure 4). Only three
207 tomograms were acquired during this faulting episode, from scan numbers 94 to 96 (Figure 2d).
208 Because of sample deformation during these scans, the 3D volumes are blurred and so we could
209 not robustly quantify the porosity. The movies S1 and S2, provided as supplementary material,
210 display time-lapse 3D rendering of the samples during the experiments.

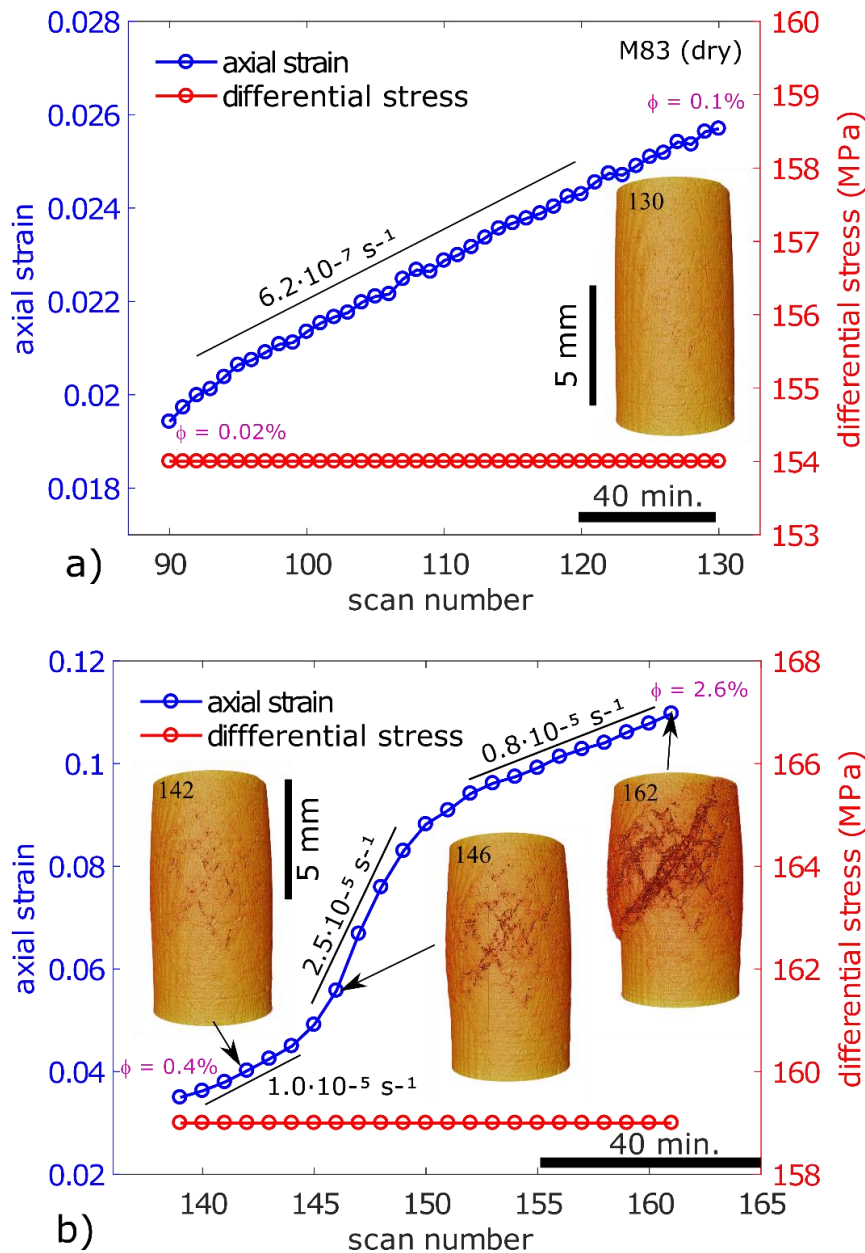
211 For both samples, we measured the macroscopic axial strain by two independent
212 techniques. First, a linear variable differential transformer (LVDT) displacement sensor installed
213 on the Hades rig measures the axial displacement of the upper piston, which records the
214 shortening of the sample (LVDT data in Figures 2b, 2d). This data is corrected from the elastic
215 deformation of the rig. Second, from the 3D tomograms we measured the height of the sample as
216 a function of time (XCT data in Figures 2b, 2d). Both measurements techniques show similar
217 results. The experiments were stopped after an axial strain of 12% (sample M83) or 60% (sample
218 M84, after failure) were reached.

219 2.3 Porosity imaging and quantification

220 Because of the contrast in X-ray attenuation between the calcite grains of the Carrara
221 marble and the air-filled voids, we can separate the microfractures and pores from the solid
222 grains (Figures 5, 6). This procedure (i.e., segmentation) allows extracting the porosity of each
223 scan. In our samples, the initial porosity detected by the segmentation procedure is less than
224 0.05%. Thus, most of the porosity that subsequently develops arises from microfracture
225 propagation. We used a simple workflow to extract the microfracture by segmenting the data of
226 sample M83. First, each tomogram was filtered using a non-local mean filter (Buades et al.,
227 2005) to reduce noise in the data and thus enhance boundaries between grains and voids. Then a
228 cylindrical mask was used to select a subvolume centered in the rock sample and comprising
229 63% of its volume, thereby reducing boundary effects by removing data near the jacket and the

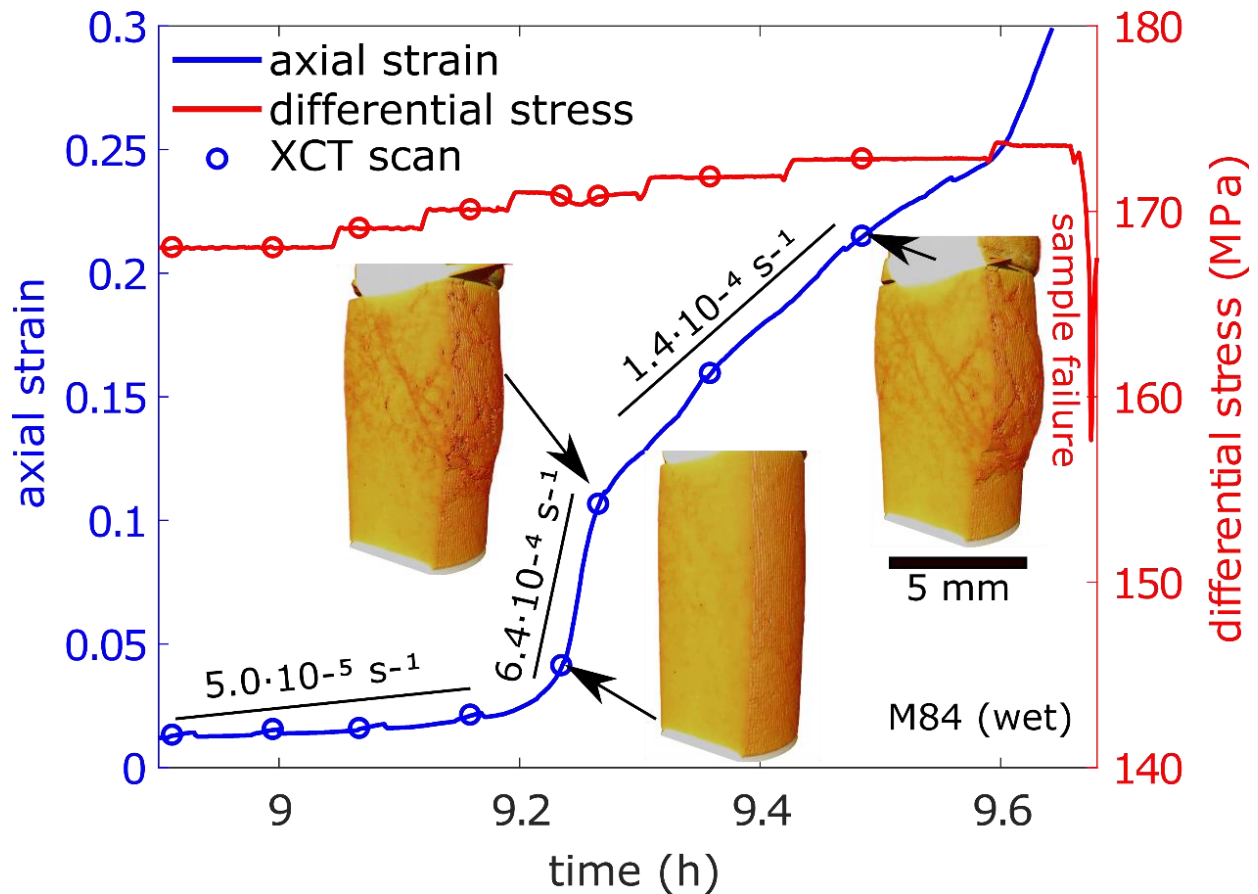
230 pistons. Then, a threshold in gray level of 13800 was applied. All voxels below this value are
 231 considered voids and all voxels above it are considered grains.

232



233

234 Figure 3: Macroscopic axial strain and differential stress for each scan acquired of sample M83
 235 (no pore fluid) in the periods indicated by gray rectangles in Figure 2a: a) The period with a
 236 linear increase of strain with time corresponds to sample deformation by secondary creep. b) The
 237 period with a transient acceleration of creep (i.e., creep burst between scans 140 and 150)
 238 corresponds to the nucleation and growth of a system-spanning fault network. Each circle
 239 indicates the acquisition of a 3D tomogram. Insets show 3D views of the sample. Horizontal
 240 black bars show a duration of 40 minutes. The porosity of the sample, ϕ , is indicated at the
 241 beginning and end of each curves.



242

243 Figure 4: Axial strain and differential stress as a function of time for sample M84 (with pore
 244 fluid) in the period indicated by gray rectangles in Figure 2b. The transient acceleration of creep
 245 (i.e., creep burst between 9.2 and 9.4 h), observed macroscopically, corresponds to the nucleation
 246 and growth of a fault network that hosts system-spanning conjugate faults, observed with X-ray
 247 tomography. Each circle indicates the acquisition of a 3D tomogram. Insets show 3D views of
 248 the sample. Local macroscopic axial strain rates are indicated above the axial strain curve.

249

250 We then calculated the evolution of porosity (Figure 7a) and the evolutions of the number
 251 of microfractures, mean volume of microfractures, and mean distance between microfractures
 252 during the creep burst (Figure 8). To characterize the spatial variability of the porosity along the
 253 axis of the core sample, we divided the tomograms into a series of vertical layers, each 130
 254 micrometers thick (20 voxels), calculated the porosity in each layer, and plotted the evolution
 255 with time (Figure 7b).

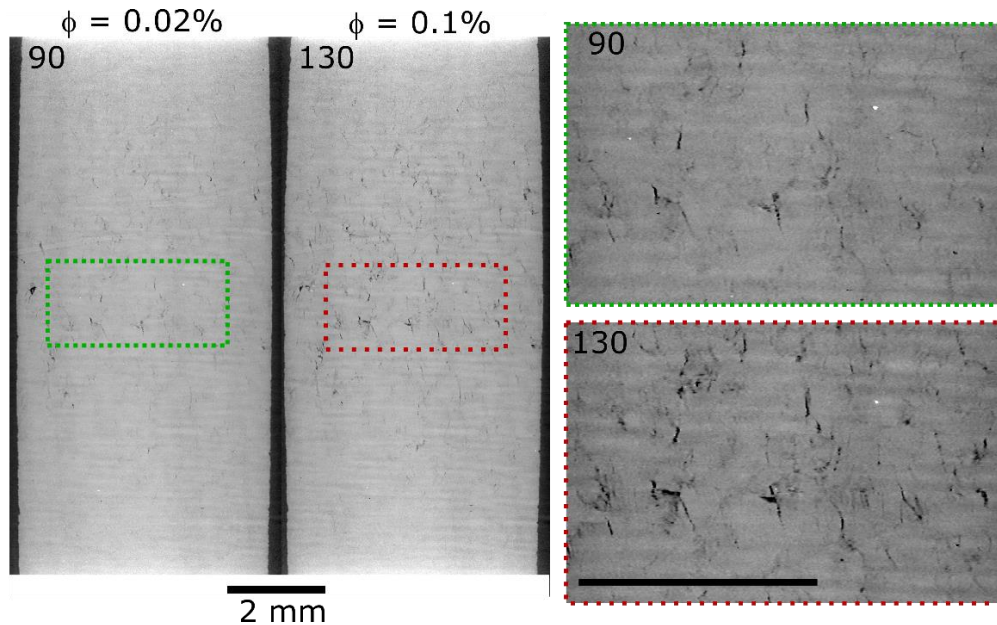
256 To characterize the shape of the microfractures (Figure 9), we calculated the covariance
 257 matrix of each microfracture, from which the three eigenvalues λ_1 , λ_2 , and λ_3 , represent the three
 258 principle axes of the microfracture (inset in Figure 9c). The mean values of these eigenvalues,
 259 the evolutions of the angle ϕ , between λ_1 and the vertical direction, and the angle ϕ_2 , between λ_3
 260 and the vertical direction are displayed in Figures 9a and 9b. We also calculated the distribution
 261 and the average of the microfracture flatness, defined by the ratio λ_3/λ_2 , with flat objects having
 262 a flatness close to zero (Figures 9c, 9d).

263 2.4 Digital volume correlation

264 To characterize the volumetric and shear strain evolution in sample M83, we calculated
 265 the incremental 3D internal displacement vectors between successive scans using digital volume
 266 correlation analysis, implemented in the software TomoWarp2 (Tudisco et al., 2017) and
 267 following the same procedure as previous analyses (McBeck et al., 2018; Renard et al., 2019).
 268 Digital volume correlation calculates the displacement vectors inside the sample at the locations
 269 of points called nodes, and uses a cubic correlation window around each node to calculate the
 270 incremental displacement done between two successive 3D scans. The node spacing was 20
 271 voxels (130 μm) and the correlation windows size was 10 voxels (130 μm).

272 Using the incremental displacement fields calculated between two tomograms, we
 273 examine both the volumetric and shear components of the strain by calculating the divergence
 274 and curl of the displacement fields, respectively. The divergence is proportional to the first
 275 invariant of the incremental strain tensor and thus represents a measurement of local volume
 276 changes. Positive divergence indicates local dilation and negative divergence indicates local
 277 contraction. The curl is a vector that characterizes the rotational component of the displacement
 278 field. The norm of this vector is used here as a proxy for incremental shear strain. In a Cartesian
 279 coordinate system where the z-axis is vertical and parallel to the core sample axis, and the x- and
 280 y-axis are perpendicular, horizontal and arbitrarily selected, a positive curl indicates right-lateral
 281 shear strain, and a negative curl indicates left-lateral shear strain with respect to the coordinate
 282 system.

283



284

285 Figure 5: Two-dimensional slices aligned parallel to the maximum compressive stress in sample
 286 M83 (dry) when the differential stress was constant and equal to 154 MPa (scan numbers 90 and
 287 130). Figure 3a shows the loading conditions of each scan. The gray scale of scans indicates X-
 288 ray attenuation, with darker shades corresponding to air-filled voids. Between these two scans,
 289 the porosity increased from 0.02% to 0.1% (Figure 3a) and the sample dilated via the nucleation
 290 and growth of microfractures. Scale bars are both 2 mm.

291

292 To visualize and quantify the strain increments we proceed in two steps. First, we show
 293 the localization patterns of the high (>95th percentile) incremental strain values (Figure 10,
 294 Movie S3). Second, we show the evolution of the cumulative values of these values with time, as
 295 deformation progresses (Figure 11). We show the cumulative values, rather than the incremental
 296 strain values, in order to compare this evolution to the trends in porosity, which is a cumulative
 297 property.

298 **3 Results**

299 **3.1 Macroscopic strain and deformation pattern**

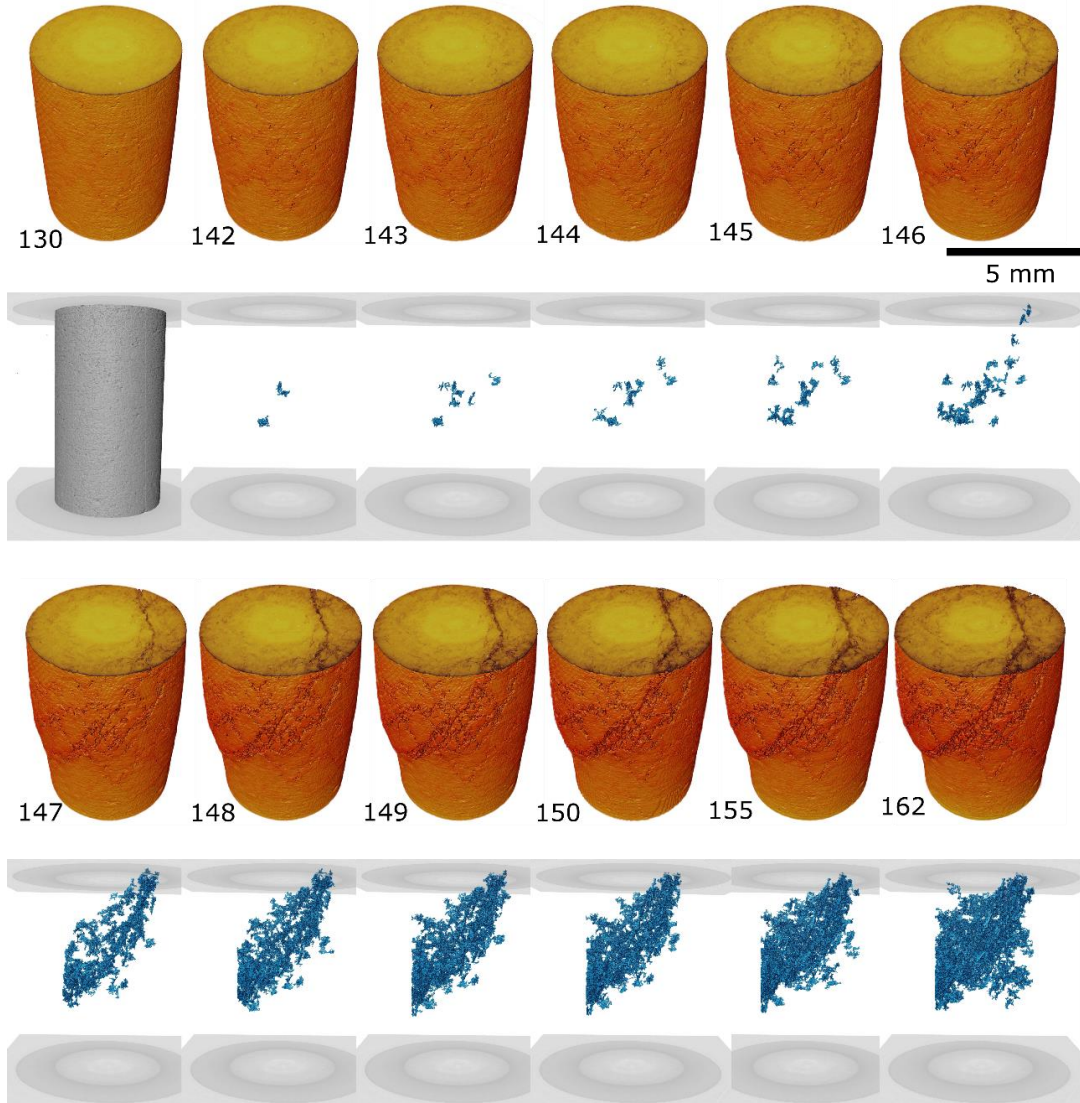
300 The macroscopic differential stress and axial strain relationships show mechanical
 301 behavior typical of a triaxial deformation test during the initial stages when axial stress was
 302 increased (Figure 2). In the first step, the differential stress versus axial strain is nonlinear,
 303 concave upward, due to the closure of voids and the settling of the sample between the two
 304 pistons. The second step includes a linear increase of axial strain with differential stress. The
 305 third stage begins when a yield point is reached after around 2-3% axial strain (Table 1),
 306 followed by a fourth stage with strain hardening during which microfractures grow under
 307 constant differential stress (Figures 2b, 2d). We defined the yield point when a deviation of 3%
 308 from linearity occurs in the stress-strain curve. The fourth and final stage includes an
 309 acceleration of macroscopic creep driven by microfracture propagation and coalescence under
 310 either constant differential stress (sample M83) or slightly increasing differential stress (M84).
 311 For both samples, conjugate sets of faults developed in the sample (insets in Figure 2, Movies
 312 S1, S2). The main difference between the two samples is that for sample M83, deformed without
 313 pore fluid, the conjugate faults developed in about forty minutes. In contrast, in sample M84,
 314 including water, the faults became system-spanning in four minutes. Because we could acquire
 315 only three scans of sample M84 (wet) during fault initiation and propagation (Movie S2), and the
 316 propagation of microfractures blurred the scans, we do not characterize the porosity and
 317 incremental strain evolution of this sample in the following analysis. We focus this analysis on
 318 sample M83 for which we acquired several tens of tomograms during creep deformation at
 319 constant differential stress (Movie S1), which did not include significant fracture propagation or
 320 deformation during scan acquisition.

321 Figure 3 shows two periods of deformation of sample M83 (dry), corresponding to the
 322 gray rectangles indicated in Figure 2a. Under a constant differential stress of 154 MPa (scans 90
 323 to 130), the sample creeps at a constant strain rate close to $6.2 \cdot 10^{-7} \text{ s}^{-1}$ (Figure 3a), between scans
 324 90 and 130. The nucleation and growth of microfractures produces the macroscopic creep
 325 (Figure 4). Twinning at the grain scale could accommodate part of the deformation. However,
 326 we could not identify this mechanism with the X-ray microtomography data. The quasi-linear
 327 trend in the increase of strain with time suggests that this stage can be defined as secondary creep
 328 (Figure 1).

329 Under a differential stress of 159 MPa (scans 139-162), an increase of axial creep rate
 330 from 10^{-5} to $2.5 \cdot 10^{-5} \text{ s}^{-1}$, defined as a creep burst, is observed from scans 140-150 (Figure 3b).
 331 The creep acceleration correlates in time with the nucleation and growth of a fault network that
 332 spans the rock core, including smaller conjugate faults (Figure 6, Movie S1). The sample-
 333 spanning fault network slips at a velocity in the range 0.4-1.8 micrometers per second, measured
 334 by the displacement along the main fault between scans 140-150. From scans 139-142, the

335 porosity increases, signaling an acceleration of fracture dilation (Figure 7a). Then the fractures
 336 that later comprise the system-spanning network begin to develop at scan 144, and continue to
 337 propagate until scan 150 (Figure 6). Between scans 150-162, the main fault network spans the
 338 system and the macroscopic strain rate decreases from $2.5 \cdot 10^{-5} \text{ s}^{-1}$ to $0.8 \cdot 10^{-5} \text{ s}^{-1}$.

339



340

341 Figure 6: Series of three-dimensional views of sample M83 during the creep burst that led to the
 342 formation of a fault network under a constant differential stress of 159 MPa. Figure 3b shows the
 343 loading conditions of each scan number. Yellow-orange cylinders show 3D views of the sample,
 344 with fractures in darker colors. Blue figures show all the microfractures with volumes greater
 345 than 10^4 voxels. Around scan 142, the number of microfractures with volume above 10^4 voxels
 346 increase. The system-spanning fault network begins to develop between scans 140 to 150,
 347 leading to the formation of an offset along the sample boundary. For scans 150-162, this offset
 348 does not increase whereas the macroscopic axial strain increases, indicating mainly volumetric
 349 deformation in the core. The time between each scan is 4 minutes.

350

351 In sample M84 (wet), the strain rate at 170 MPa differential stress is equal to $5.0 \cdot 10^{-5} \text{ s}^{-1}$
 352 and deformation occurs by the nucleation of microfractures in the volume (Figure 4). After 9.2
 353 hours, a creep burst starts with a strain rate of $6.4 \cdot 10^{-4} \text{ s}^{-1}$ and lasts for four minutes. During this
 354 period, several conjugate faults develop and accommodate most of the deformation. The slip rate
 355 measured on the main faults, using the tomography data, between 9.24 and 9.28 hours is in the
 356 range 1.5-2.5 micrometers per second. After this creep burst, the strain rate decreases to $1.4 \cdot 10^{-4}$
 357 s^{-1} until the sample failed at 9.7 hours (Figure 4).

358

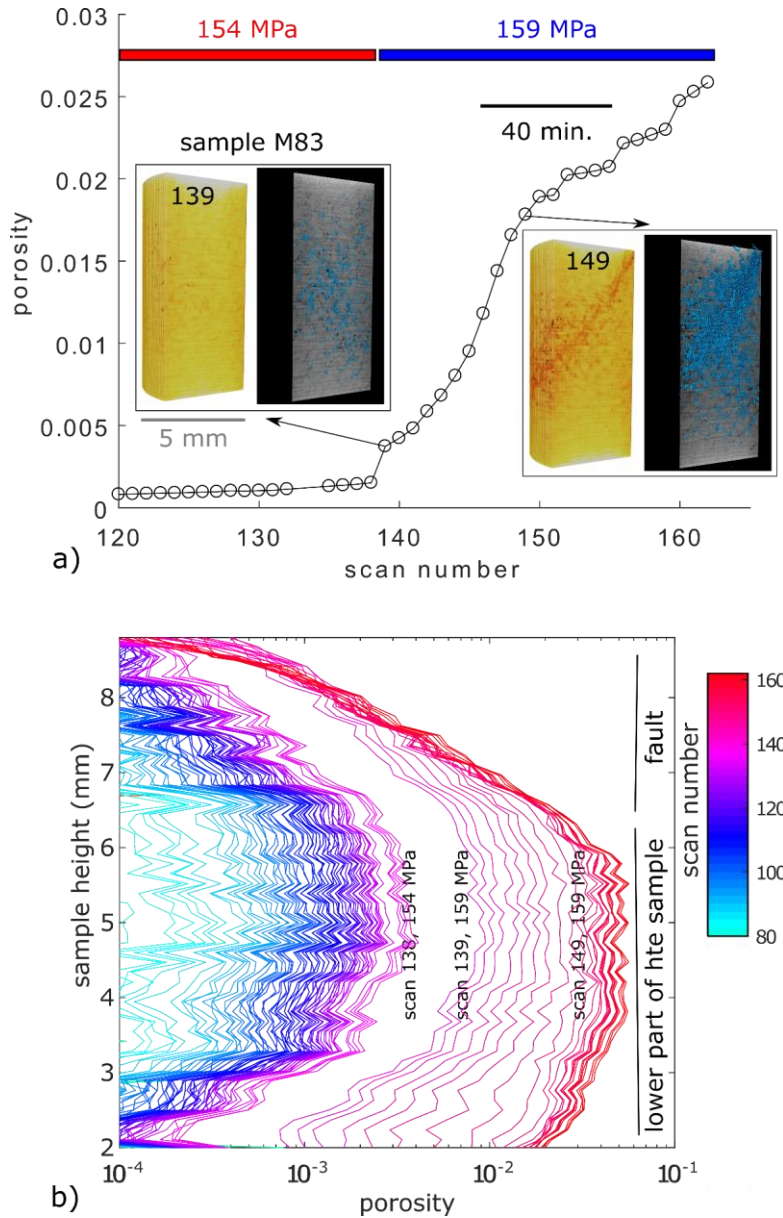
359 3.2 Evolution of porosity

360 The porosity in sample M83 (dry) evolves during deformation (Figure 7).
 361 Microtomography reveals that fault growth occurs as the formation of a zone of increased
 362 porosity in the top half of the sample (Figures 6, 7a). This dilating volume propagates across the
 363 sample until it reaches the boundary of the rock core. The porosity of the entire sample increases
 364 from less than 0.5% before deformation to 2.5% after the fault network spans the core (Figure
 365 7a). After the fault network has crossed the sample, the strain rate decreases. The time evolution
 366 of the porosity along a vertical profile in the sample shows that porosity increases mainly in the
 367 middle of the sample, far from the two pistons (Figure 7b). Above the fault network, the porosity
 368 increases with time during fault propagation (scans 139-150) and then stops increasing. Porosity
 369 continues to increase in the lower part of the sample (scans 150-162), below the fault network,
 370 after it has stopped propagating.

371 Segmenting the voids (fracture and pores) from the solid rock produce evolving statistics
 372 of microfracture geometry (Figures 8, 9). During the steady-state creep stage (scans 90-130 in
 373 Figure 3a), the mean values of the three eigenvalues of the covariance matrix, λ_1 , λ_2 , and λ_3 ,
 374 increase slowly (Figure 9a). Idealizing a microfracture as a perfect ellipsoid, the three
 375 eigenvalues correspond to the three main axes of the ellipsoid, with the smallest eigenvalue, λ_3 ,
 376 corresponding to the fracture aperture. During scans 90-130, a phase a secondary creep before
 377 the creep burst, the average angle between the largest principle axis of the microfractures, λ_1 , and
 378 the horizontal plane, ϕ , remains constant, around 64° (Figure 9b). The angle between the smallest
 379 principle axis of the microfractures (λ_3) and a horizontal plane, ϕ_2 , also remains constant, above
 380 70° . This high value of the angle ϕ_2 indicates that the smallest dimensions of the microfractures
 381 is almost perpendicular to the vertical direction, and thus that the long axes of the microfractures
 382 are oriented almost parallel to σ_1 . The flatness, corresponding to the ratio between the smallest
 383 and the intermediate eigenvalues of the microfractures is constant and equal to 0.2 (Figure 9c),
 384 indicating that the microfractures are generally flat objects, with a geometry similar to that of a
 385 penny shape.

386 During the stage of the experiment with the fastest rate of macroscopic creep (scans 139-
 387 150 in Figure 3b), i.e., the creep burst, the number and mean volume of microfractures increase
 388 (Figure 8). As a consequence, the mean distance between microfractures decreases (Figure 8b).
 389 The three eigenvalues of the microfractures and their flatness increase (Figures 9a, 9c, 9d). This
 390 observation indicates that the microfractures grow in length and width, explaining the increase of
 391 porosity and thus dilatancy. Concurrently, the mean orientation of the microfractures evolves: the
 392 angle ϕ increases to 68° , while the angle ϕ_2 decreases to 60° (Figure 9b). Because the flatness of
 393 the voids is small, less than 0.3, these voids have a flat shape with $\lambda_1, \lambda_2 \gg \lambda_3$. With such
 394 geometry, the longest axis of the voids could be either vertical or horizontal, with an angle ϕ than

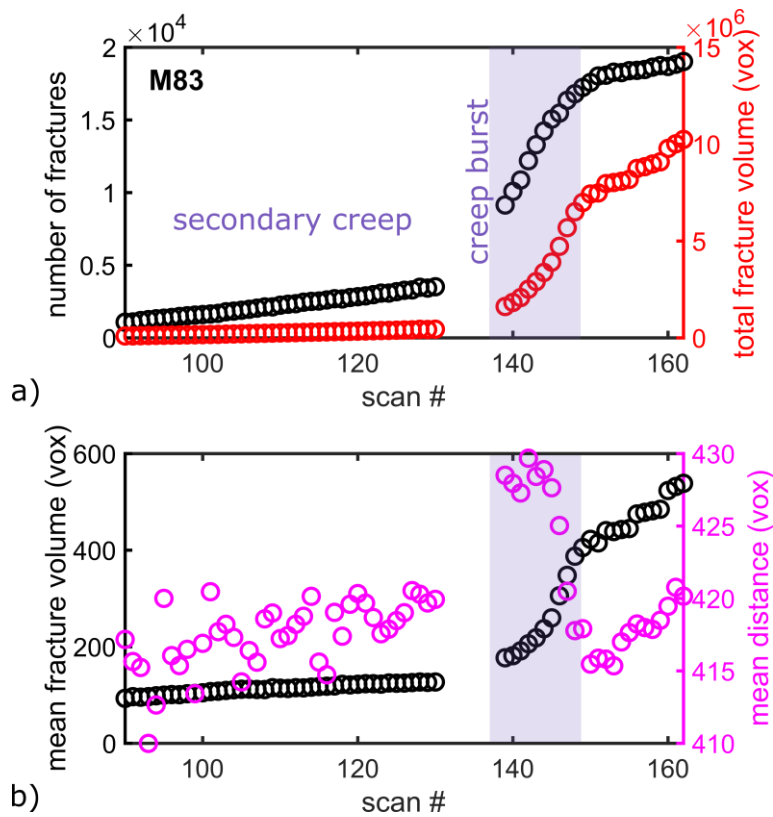
395 can therefore be either close to 90° or close to 0° for a vertical microfracture. Therefore, the
 396 angle ϕ_2 of the smallest axis, λ_3 , is the most relevant geometrical parameter to estimate the
 397 orientation of penny-shaped microfractures. High angles of ϕ_2 indicates that the aperture of the
 398 fracture is perpendicular to σ_1 , or that the penny-shaped fracture is close to being vertical (inset
 399 in Figure 9b). The evolution of ϕ_2 observed on Figure 9b shows a rotation of the microfracture
 400 orientation, with the smallest dimension oriented at 60° to σ_1 . This orientation corresponds to
 401 one of the other two axes of the microfractures oriented at 30° to σ_1 , the optimal orientation for
 402 shear faulting when considering an internal friction coefficient equal to 0.6 (Anderson, 1905).
 403



404
 405 Figure 7: a) Evolution of porosity in sample M83 as a function of scan number during fault
 406 network development. Insets show a three-dimensional rendering (left) where color intensity
 407 represents X-ray attenuation (darker shades correspond to pores, with less attenuation) and

408 segmentation of the pores (right, porosity in blue) at two time steps. Before fault network growth
 409 (scan 139), porosity is mainly concentrated in the central part of the sample. After the network
 410 reaches the sample boundaries (scan 149), porosity becomes concentrated around the fault plane.
 411 The jump in porosity between scans 138 and 139 is due to an increase of imposed differential
 412 stress from 154 to 159 MPa. b) Evolution of porosity with time (scan number) along the vertical
 413 axis of the sample. The porosity increases mostly in the middle of the sample and less near the
 414 pistons at the top and bottom boundaries. After scan 139, the differential stress remained
 415 constant until the end of experiment (scan 162). The fault network developed in the upper part of
 416 the sample (scans 139-149), while porosity continued to increase in the lower part of the sample
 417 and we interpret that shearing prevented porosity increase in the fault.

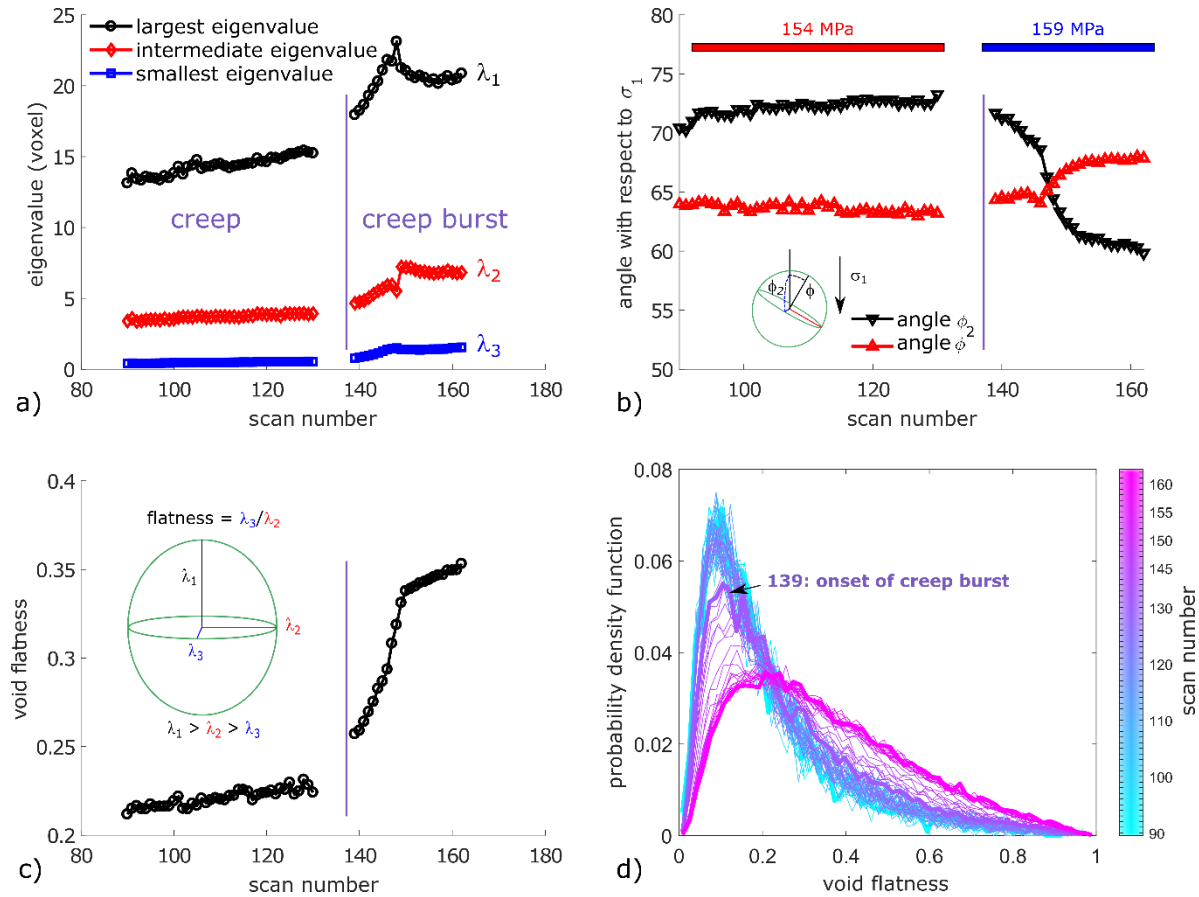
418



419

420 Figure 8: Evolution of the number of microfractures and total microfracture volume (a), and the
 421 mean microfracture volume and mean distance between microfractures (b) as a function of scan
 422 number. During the secondary creep phase, the total number of fracture increases, whereas the
 423 total fracture volume remains constant. During the creep burst (scans 139-150, shaded rectangle),
 424 the number and the mean volume of microfractures increase whereas the mean distance between
 425 microfractures decreases. Following the creep burst, the number of fractures, mean fracture
 426 volume, and mean distance between fractures all tend to plateau, indicating the slowing or
 427 stalling of fracture network development (i.e., fault locking).

428



429
 430 Figure 9: Statistics of microfracture geometry between a period of slower creep when the
 431 differential stress was constant and equal to 154 MPa (scans 90-130) and faster creep (i.e., creep
 432 burst) when the differential stress was constant and equal to 159 MPa (scans 139-162). a)
 433 Evolution of the average lengths of the three principle eigenvalues of the covariance matrix of all
 434 microfractures in the sample, $\lambda_1 > \lambda_2 > \lambda_3$. During the creep burst, all three values increase
 435 indicating that microfractures grow along each dimension. b) Evolution of the average angles ϕ
 436 and ϕ_2 between the horizontal axis and λ_1 and λ_3 , respectively. The evolution of the angle ϕ_2
 437 during the creep burst indicates that the smallest axis of the microfractures become oriented at an
 438 angle of 60° with respect to σ_1 , indicating that the microfractures' planes tend to become
 439 oriented at 30° , a direction more favourable for shear slip. c) The average flatness of the fractures
 440 increases with deformation, indicative of crack opening. A small value of flatness, defined as the
 441 ratio between the smallest and intermediate eigenvalues, indicates a flat, penny-shaped object.
 442 The inset shows a microfracture, approximated by an ellipsoid and the three eigenvalues of the
 443 covariance matrix, which correspond to the three main axes of the ellipse. d) Evolution of the
 444 probability density function of the flatness. The mean flatness increases with time, indicative of
 445 crack opening. Scan number 139 corresponds to the onset the creep burst, where the flatness
 446 starts increasing.

447

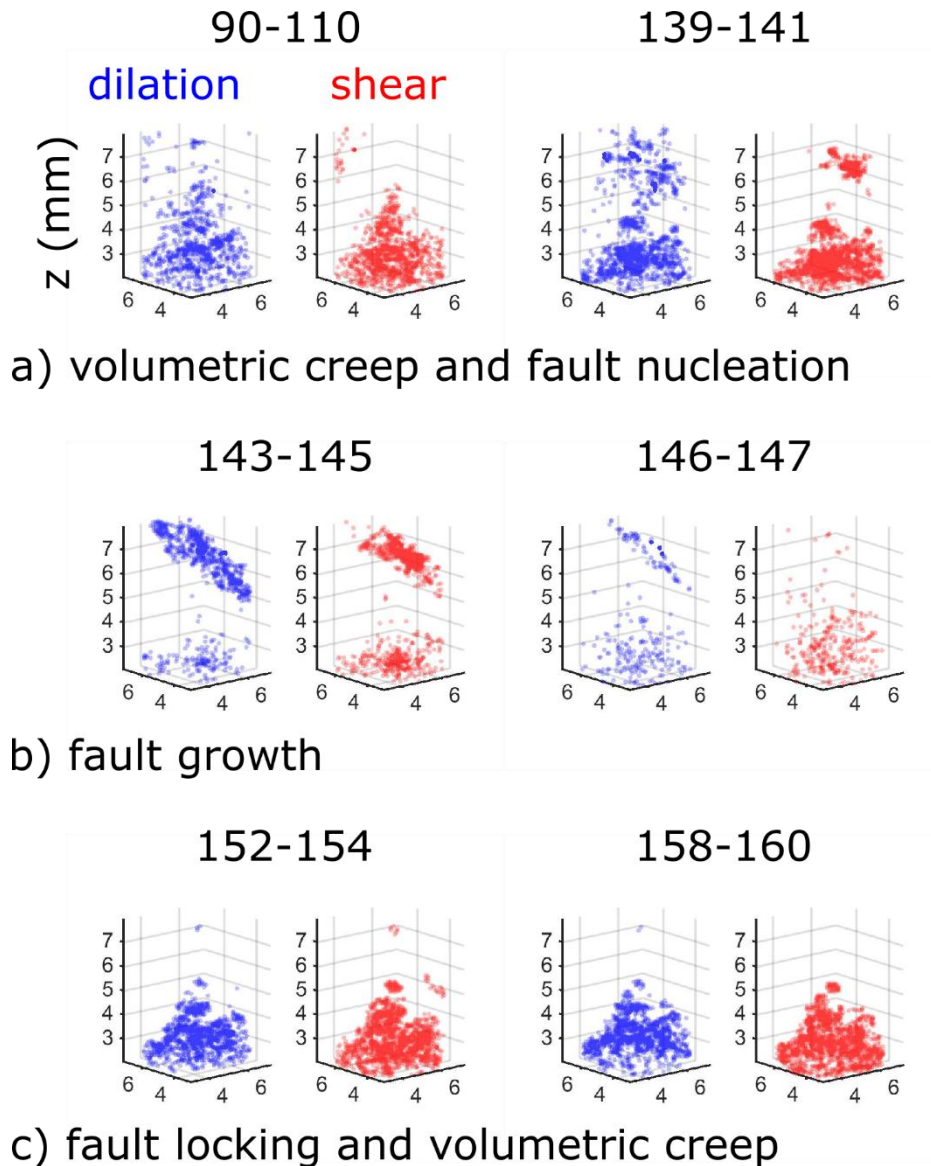
448 3.3 Local strain accumulation

449 Digital volume correlation analysis characterizes the incremental volumetric and shear
 450 strains during creep deformation. In sample M83 (dry), the highest magnitudes of the

451 incremental local strain ($>95^{\text{th}}$ percentile) occurred pervasively in the volume and did not
452 become localized until scan 141. In particular, between scans 90-140, high magnitudes of
453 dilation and shear strain concentrated in the lower half of the sample (Figure 10a). During this
454 period, the number of microfractures increased but the total volume of fractures did not increase
455 significantly (Figure 8a). As the fault network nucleated, a band of high magnitudes of dilation,
456 and a more localized zone of shear strain, formed in the upper part of the sample (Figure 10a,
457 between scans 139-141, Movie S3). Then, larger volumes of high dilation and shear strain
458 developed along the system-spanning fault network between scans 145 and 149 (Figure 10b).
459 Then, slip along the fault slowed as well as the rate of new fault propagation (Figure 8a), and the
460 highest magnitudes of incremental deformation occurred mostly in the lower part of the sample
461 (Figure 10c) between scans 150 and 162. This increase of incremental shear strain (i.e. creep
462 burst) corresponds to the development of the sample-spanning fault network (Figure 6) and the
463 increase of porosity in the fault zone (Figure 7b) At the same time, the number of microfractures
464 increased as well as their volume (Figure 8), The mean distance between microfracture centroids
465 increased as well, indicative of a global dilation in the fault zone. Once the fault locked, after
466 scan 150, the porosity continued to increase, mainly in the lower part of the sample (Figure 7b).

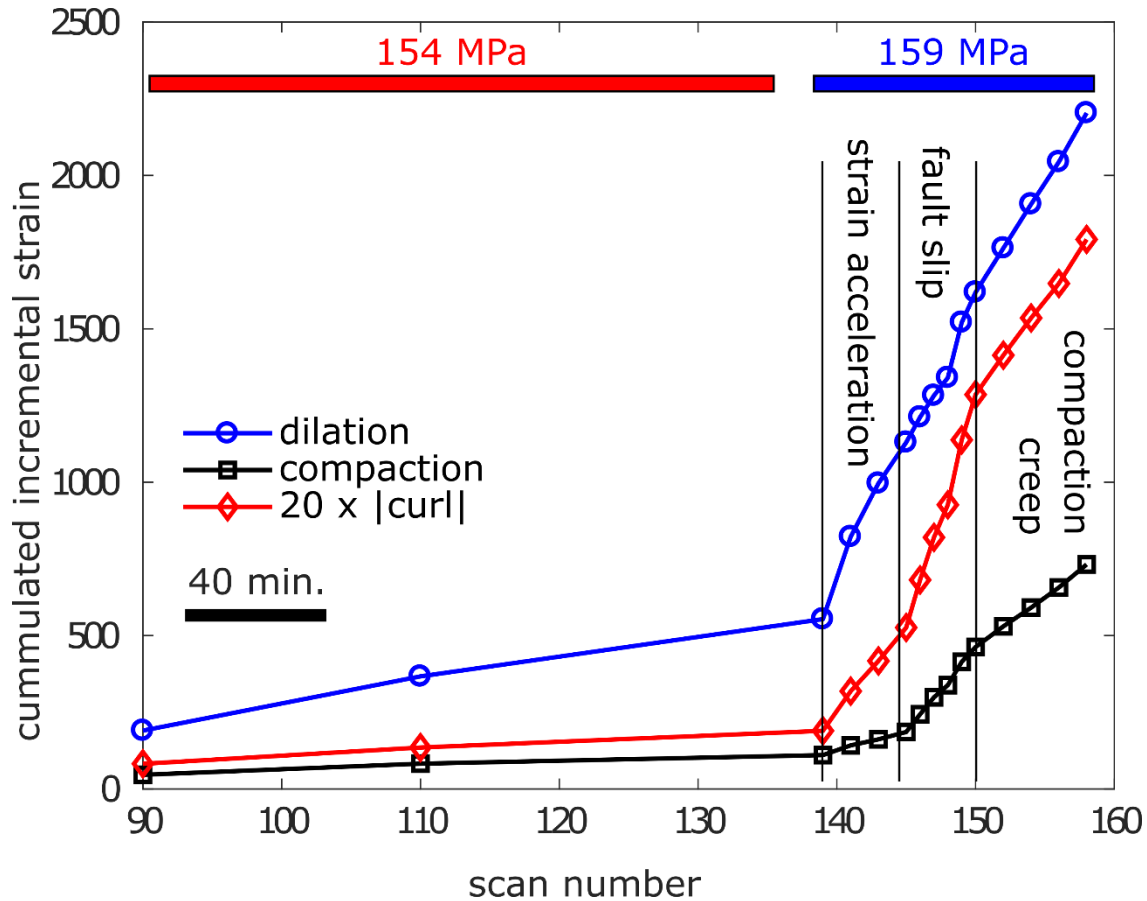
467 To characterize the accumulation of incremental strain in the sample, we calculate the
468 evolution of the cumulative values of dilation, compaction, and curl. First, we sum all these
469 values in each DVC calculation. Then, we sum cumulatively between successive scans. This
470 procedure allows comparing the DVC results with porosity evolution. This cumulative sum over
471 time of dilation and shear increments show a similar evolution (Figure 11). From scans 90 to
472 141, the cumulative dilation increases in the sample, while the shear strain magnitudes remain
473 low. Then the cumulative dilation increases, as well as compaction and shear strain between
474 scans 141 to 145, concurrent with the porosity increase in the sample. From scans 145 to 149,
475 both dilation and shear strain accelerates, corresponding to the growth and slip on the sample-
476 spanning fault. After scan 150, slip on the fault decreases and both cumulative volumetric and
477 shear strain continue to increase at a smaller rate in the lower part of the sample (Figure 10c).

478 These data show that the acceleration of macroscopic creep observed between scans 141
479 and 150 occurred by 1) dilation of the sample along a nascent shear zone, 2) propagation of this
480 shear zone as a quasi-planar structure that crossed the sample and slipped, 3) the slowing of slip
481 on this fault network, slowing of the rate of fracture nucleation and diffuse deformation in the
482 rock volume around it. This microscopic evolution characterizes the macroscopic creep bursts
483 observed in the local strain data (Figure 3b).



484

485 Figure 10: Local incremental strains calculated between pairs of tomograms acquired of sample
 486 M83. The numbers above each plot indicate the pair of tomograms used for the calculation.
 487 Distance units are given in mm. Colored circles show the highest 95th percentile of the
 488 incremental positive divergence (dilation, blue) and absolute value of curl (shear, red). a) Before
 489 fault network nucleation, high magnitudes of dilation and shear strain develop at the bottom of
 490 the sample. At the onset of fault network nucleation, high magnitudes of dilation and shear begin
 491 to concentrate in the top part of the sample. b) During fault network propagation across the
 492 sample, dilation dominates the volume of the future fault plane, while the high magnitudes of
 493 shear are confined to a smaller volume. c) After some time, the fault locks, accommodating
 494 lower magnitudes of strain (<95th percentile), and volumetric deformation at the bottom of the
 495 sample accommodates creep. The Figures 3b and 6 show the axial strain and 3D views of the
 496 sample. The Movie S3 shows the complete evolution of the incremental dilation, contraction, and
 497 shear strain.



498

499 Figure 11: Cumulative strain evolution at constant differential stress conditions (154 or 159
500 MPa) in sample M83 before, during and after the creep burst. The black bar indicates the time
501 scale. The black vertical lines mark the onset of the acceleration of dilation, compaction, and
502 shear (the onset of the creep burst at scan 139), the onset of fault nucleation and slip, and the
503 period where strain was accommodated by volumetric compaction creep in the lower part of the
504 sample and not only localized along the fault.

505

506 4 Discussion

507 4.1 Creep in Carrara marble

508 Our experimental results share similarities with previous experiments of brittle creep in
509 Carrara marble. At high temperature, above 400°C, several mechanisms produce creep of
510 Carrara marble including the formation of twins, grain boundary sliding and activation of
511 dislocation displacements (e.g., Quintanilla-Terminel and Evans, 2016). However, at lower
512 temperature, the creep mechanism in marble is mainly due to the growth and coalescence of
513 microfractures (Tal et al., 2016). Triaxial creep experiments with cyclic loading on marble at
514 room temperature have shown that the macroscopic axial strain increases with time with a
515 slightly nonlinear trend, under a differential stress loading equal to 60% of the short term
516 strength of the material (Figure 7 in Yang et al., 2015). Two different viscous dissipation
517 processes were proposed by these authors that could produce this nonlinearity: a visco-elastic

518 term with an exponential dependence in time and a visco-plastic term with a linear dependence
519 in time.

520 Below 50% of the differential stress at macroscopic failure, creep in marble was below
521 the detection limit of triaxial compression laboratory experiments (Liu et al., 2017). At room
522 temperature, 30 MPa confining pressure and 150 MPa differential stress, the creep rate of Jinping
523 Bed marble in China was close to 10^{-7} s^{-1} (Liu et al., 2017). For other marble samples from the
524 same area, the creep strain rate measured at 35 MPa confining pressure, 145 MPa differential
525 stress, and room temperature, was smaller, around $2 \cdot 10^{-8} \text{ s}^{-1}$ (Yang et al., 2015). In our
526 experiments, the steady state creep rate before the creep burst is in the range $6.2 \cdot 10^{-7}$ - $5.0 \cdot 10^{-5} \text{ s}^{-1}$
527 under constant differential stress and room temperature (Figure 3a). These values are slightly
528 higher than those reported by Yang et al. (2015) and Liu et al (2017), probably because our creep
529 rates are measured at a differential stress closer to failure than in their experiments. However, the
530 main difference is that we observed creep bursts in our data, with strain rates in the range $2.5 \cdot 10^{-5}$ -
531 $6.4 \cdot 10^{-4} \text{ s}^{-1}$ (Figure 3b), several orders of magnitude larger than creep rates previously reported
532 in marble (e.g., Yang et al., 2015; Liu et al., 2017).

533 4.2 Brittle creep and faulting in rock experiments

534 Other laboratory experiments performed on crystalline low porosity rocks have measured
535 strain rates during brittle creep. Lockner (1993) deformed granite samples at room temperature,
536 under constant confining and pore pressure conditions, as the axial stress was cycled to enhance
537 creep. Macroscopic axial strain increases with a linear dependence of time when the applied
538 differential stress is at some distance (80%) of the failure stress, i.e., secondary creep (Figure 1).
539 This secondary creep strain rate follows an exponential dependence with the applied (constant)
540 stress (Lockner, 1993). From the recording of acoustic emissions and post-mortem observations
541 of microfractures, the nucleation and subcritical growth of microfractures have been identified as
542 dominant microstructural mechanisms that accumulate irreversible strain (Lockner, 1993; Ross
543 et al., 1983; Scholz, 1968). In our experiments, steady state creep occurs under a differential
544 stress of 154 MPa in sample M83 (scans 90-130) and coincides in time with the nucleation and
545 growth of microfractures (Figures 3a, 5). During this deformation stage, the porosity increases
546 slightly (Figure 3a). The average shape of microfracture remains similar, and their orientation is
547 consistently near parallel to σ_1 with an angle ϕ_2 close to 70° (Figure 9). These dilatant vertical
548 cracks formed in the sample produce irreversible damage. With continuing creep, when
549 approaching fault formation, these microfractures coalesced to form a fault network that
550 extended across the sample. These stages of fracture coalescence were also observed in 2D
551 experiments on Carrara marble (Tal et al., 2016).

552 In a series of experiments on crystalline rock performed under constant differential stress,
553 Lei et al. (2000) measured a non-linear increase of the rate of acoustic emissions that occurred
554 within one minute in a rock sample loaded near failure. The spatial distribution of the acoustic
555 emissions indicates that they were initially distributed throughout the rock and then concentrated
556 in a quasi-planar structure that evolved into a more localized fault. The zone with tensile
557 fracturing located in front of the propagating fault, identified from acoustic emission recording,
558 supports the existence of a dilatant process zone. The fault then propagates within this process
559 zone, a mechanism proposed in Reches and Lockner (1994). In porous rocks, such as sandstone,
560 acoustic emission recording show that creep remains diffuse in the volume, without localizing
561 into a sub-planar structure (Heap et al., 2009). In the creep burst reported in the present study,

562 strain localization occurs initially in the formation of a dilatant (high porosity) zone in the middle
563 of the sample (Figures 6 and 10, scans 143-145), with low magnitudes of cumulative shear strain
564 (Figure 11), and higher local porosity increase. Then high magnitudes of shear strain localized
565 into a system-spanning fault (scans 143-147 in Figure 10). After the fault network crossed the
566 sample, slip along it decreased, the rate of fracture propagation slowed, and creep continued in
567 the lower half of the core (Figures 7b, 8, 10c, scans 150-162).

568 The development of faults in laboratory creep experiments has been observed in granite
569 (Lei et al., 2000) and basalt (Heap et al., 2011). In amphibolite (Sato et al., 1996), a fault
570 developed along a pre-existing joint that acted as a nucleation site for localized deformation. In
571 these experiments on granite, basalt and amphibolite, an increase of the number and the energy
572 of acoustic emissions occurred when approaching failure. This increase was interpreted as the
573 development of microfractures at the grain scale. In experiment M83 (dry), we directly observe
574 that fault growth occurs slowly, with varying rates of creep, rather than a faster evolution toward
575 catastrophic failure. Moreover, once the fault network spans the system, slip on it decreased, and
576 creep deformation was accommodated in the lower part of the sample by the opening of new
577 microfractures, rather than through accelerating slip along this through-going fault network.
578 Conversely, in sample M84 (wet), the creep burst precedes macroscopic failure, and occurred
579 during the tertiary creep phase.

580 An important difference between our two experiments is that the macroscopic strain rate
581 during the creep burst is around 25 times faster in sample M83 (wet) (Figure 3b), than for sample
582 M84 (dry) (Figure 4). The influence of water on accelerated creep has also been observed in
583 granite (Krantz, 1982), sandstone (Baud et al., 2000), and single calcite crystals (Røyne et al.,
584 2011). The presence of water lowers the surface energy between calcite and water during
585 fracture propagation, producing the faster rate of fracture growth, as observed in sample M84.

586 **5 Conclusions**

587 The experiments reported in the present study indicate that, under constant stress
588 conditions at room temperature, cores of Carrara marble deform macroscopically in creep due
589 mainly to the growth of microfractures. Both secondary and tertiary creep occur in the
590 experiments (Figure 1). The stage of tertiary creep includes creep bursts: transient accelerations
591 of creep, similar to slow slip events measured on continental faults that have been interpreted as
592 an acceleration of slip along a pre-existing fault plane (Linde et al., 1996; Jolivet et al., 2013;
593 2015, Rousset et al., 2016). In our experiment, the creep bursts did not occur on a pre-existing
594 fault, but coincided with the development of a system-spanning connected fault network. At the
595 microscale, the creep burst coincides in time with the 1) localization of fractures along a quasi-
596 planar structure, 2) increase of the aperture of the microfractures, 3) rotation of the orientation of
597 the microfractures to 30° to σ_1 , more favorable for shear deformation, and 4) localization of the
598 highest magnitudes of the local dilation and shear strain into a sub-planar inclined structure.
599 Once formed, slip on the fault network decreased, the high magnitudes of strain delocalized from
600 this fault zone, the rate of fault propagation slowed, and creep continued in the volume around
601 the fault. Our results therefore demonstrate that creep bursts in laboratory experiments may
602 indicate the birth of a new fault, and not only an acceleration of transient slip on a pre-existing
603 fault which is the common explanation for slow slip events observed in active faults.

604

605 **Acknowledgments and Data**

606 We thank Elodie Boller, Paul Tafforeau, and Alexander Rack for providing advice on the design
 607 of the tomography setup, and Sanchez Technology for building the deformation apparatus. The
 608 authors received funding from the Norwegian Research Council (grant 272217). X-ray
 609 tomography data of the two experiments will be available on Norstore
 610 (<https://archive.norstore.no/>) at the time of publication of the present study.

611

612 **References**

- 613 Amitrano, D., & Helmstetter, A. (2006), Brittle creep, damage, and time to failure in rocks,
 614 *Journal of Geophysical Research*, 111, B11201, doi:10.1029/2005JB004252.
- 615 Anderson, E. M. (1905), The dynamics of faulting. *Transactions of the Edinburgh Geological*
 616 *Society*, 8(3), 387-402.
- 617 Aslan, G., Lasserre, C., Cakir, Z., Ergintav, S., Özarparci, S., Dogan, U., Bilham, R., & Renard,
 618 F. (2019), Shallow creep along the 1999 Izmit Earthquake rupture (Turkey) from GPS
 619 and high temporal resolution interferometric synthetic aperture radar data (2011–2017).
 620 *Journal of Geophysical Research: Solid Earth*, 124(2), 2218-2236.
- 621 Baud, P., Zhu, W., & Wong, T.-F. (2000), Failure mode and weakening effect of water on
 622 sandstone. *Journal of Geophysical Research*, 105 (B7), 16371-16389.
 623 doi:10.1029/2000JB900087.
- 624 Baud, P., & Meredith, P. G. (1997), Damage accumulation during triaxial creep of Darley Dale
 625 sandstone from pore volumetry and acoustic emission. *International Journal of Rock*
 626 *Mechanics and Mining Sciences*, 34(3-4), 24-e1.
- 627 Bouchon, M., Karabulut, H., Aktar, M., Özalaybey, S., Schmittbuhl, J., & Bouin, M. P. (2011),
 628 Extended nucleation of the 1999 Mw 7.6 Izmit earthquake, *Science*, 331(6019), 877-880.
- 629 Brace, W. F., Paulding Jr., B. W., & Scholz, C. H. (1966), Dilatancy in the fracture of crystalline
 630 rocks, *Journal of Geophysical Research*, 71, 3939–3953.
- 631 Brantut, N., Heap, M. J., Meredith, P. G., & Baud, P. (2013), Time-dependent cracking and
 632 brittle creep in crustal rocks: A review. *Journal of Structural Geology*, 52, 17-43.
- 633 Buades, A., Coll, B., & Morel, J. M. (2005), A non-local algorithm for image denoising. In
 634 Computer Society Conference on Computer Vision and Pattern Recognition, 2005, IEEE
 635 vol. 2, pp. 60-65.
- 636 Bürgmann, R. (2018), The geophysics, geology and mechanics of slow fault slip. *Earth and*
 637 *Planetary Science Letters*, 495, 112-134.
- 638 Carlà, T., Intrieri, E., Raspini, F., Bardi, F., Farina, P., Ferretti, A., Colombo, D., Novali, F., &
 639 Casagli, N. (2019), Perspectives on the prediction of catastrophic slope failures from
 640 satellite InSAR. *Scientific Reports*, 9(1), 1-9.
- 641 Cox, S. J. D., & Scholz, C. H. (1988), Rupture initiation in shear fracture of rocks: an
 642 experimental study. *Journal of Geophysical Research: Solid Earth*, 93(B4), 3307-3320.

- 643 French, M. E., & Zhu, W. (2017), Slow fault propagation in serpentinite under conditions of high
644 pore fluid pressure. *Earth and Planetary Science Letters*, 473, 131-140.
- 645 Gratier, J. P., Dysthe, D. K., & Renard, F. (2013), The role of pressure solution creep in the
646 ductility of the Earth's upper crust. In *Advances in Geophysics* (Vol. 54, pp. 47-179).
647 Elsevier.
- 648 Griggs, D. (1939), Creep of rocks. *The Journal of Geology*, 47(3), 225-251.
- 649 Griffith, W. A., Nielsen, S., Di Toro, G., & Smith, S. A. F. (2010), Rough faults, distributed
650 weakening, and off-fault deformation, *Journal of Geophysical Research*, 115, B08409,
651 doi:10.1029/2009JB006925.
- 652 Guglielmi, Y., Cappa, F., Avouac, J. P., Henry, P., & Elsworth, D. (2015), Seismicity triggered
653 by fluid injection-induced aseismic slip. *Science*, 348(6240), 1224-1226.
- 654 Handwerger, A. L., Huang, M. H., Fielding, E. J., Booth, A. M., & Bürgmann, R. (2019), A shift
655 from drought to extreme rainfall drives a stable landslide to catastrophic failure. *Scientific*
656 *Reports*, 9(1), 1-12.
- 657 Heap, M. J., Baud, P., Meredith, P. G., Bell, A. F., & Main, I. G. (2009), Time-dependent brittle
658 creep in Darley Dale sandstone, *Journal of Geophysical Research*, 114, B07203,
659 doi:10.1029/2008JB006212.
- 660 Heap, M. J., Baud, P., Meredith, P. G., Vinciguerra, S., Bell, A. F., & Main, I. G. (2011), Brittle
661 creep in basalt and its application to time-dependent volcano deformation. *Earth and*
662 *Planetary Science Letters*, 307(1-2), 71-82.
- 663 Jolivet, R., Lasserre, C., Doin, M. P., Peltzer, G., Avouac, J. P., Sun, J., & Dailu, R. (2013),
664 Spatio-temporal evolution of aseismic slip along the Haiyuan fault, China: Implications
665 for fault frictional properties. *Earth and Planetary Science Letters*, 377, 23-33.
- 666 Jolivet, R., Candela, T., Lasserre, C., Renard, F., Klinger, Y., & Doin, M. P. (2015), The burst-
667 like behavior of aseismic slip on a rough fault: The creeping section of the Haiyuan fault,
668 China. *Bulletin of the Seismological Society of America*, 105(1), 480-488.
- 669 Kandula, N., Cordonnier, B., Boller, E., Weiss, J., Dysthe, D. K., & Renard, F. (2019), Dynamics
670 of microscale precursors during brittle compressive failure in Carrara marble. *Journal of*
671 *Geophysical Research: Solid Earth*, 124(6), 6121-6139.
- 672 Kie, T. T., Quan, S. Z., Hai, Y. Z., & Yang, W. X. (1989), Dilatancy, creep and relaxation of
673 brittle rocks measured with the 8000 kN multipurpose triaxial apparatus. *Physics of the*
674 *Earth and Planetary Interiors*, 55(3-4), 335-352.
- 675 Kranz, R. L., & Scholz, C. H. (1977), Critical dilatant volume of rocks at the onset of tertiary
676 creep. *Journal of Geophysical Research*, 82(30), 4893-4898.
- 677 Kranz, R. L. (1980), The effects of confining pressure and stress difference on static fatigue of
678 granite. *Journal of Geophysical Research: Solid Earth*, 85(B4), 1854-1866.
- 679 Kranz, R.L., Harris, W.J., & Carter, N.L. (1982), Static fatigue of granite at 200 °C. *Geophysical*
680 *Research Letters*, 9 (1), 1-4. doi:10.1029/GL009i001p00001.
- 681 Linde, A. T., Gladwin, M. T., Johnston, M. J., Gwyther, R. L., & Bilham, R. G. (1996), A slow
682 earthquake sequence on the San Andreas fault. *Nature*, 383(6595), 65-68.

- 683 Liu, Z., & Shao, J. (2017), Strength behavior, creep failure and permeability change of a tight
684 marble under triaxial compression. *Rock Mechanics and Rock Engineering*, 50(3), 529-
685 541.
- 686 Lockner, D., & Byerlee, J. (1977), Acoustic emission and creep in rock at high confining
687 pressure and differential stress. *Bulletin of the Seismological Society of America*, 67(2),
688 247-258.
- 689 Lockner, D. (1993). Room temperature creep in saturated granite, *Journal of Geophysical*
690 *Research*, 98(B1), 475– 487, doi:10.1029/92JB01828.
- 691 Lohman, R. B., & McGuire, J. J. (2007), Earthquake swarms driven by aseismic creep in the
692 Salton Trough, California. *Journal of Geophysical Research: Solid Earth*, 112(B4).
- 693 Lomnitz, C. (1956), Creep measurements in igneous rocks. *The Journal of Geology*, 64(5), 473-
694 479.
- 695 Main, I. G. (1999), Applicability of time-to-failure analysis to accelerated strain before
696 earthquakes and volcanic eruptions. *Geophysical Journal International*, 139(3), F1-F6.
697 doi:10.1046/j.1365-246x.1999.00004.x.
- 698 Main, I. G. (2000), A damage mechanics model for power-law creep and earthquake aftershock
699 and foreshock sequences. *Geophysical Journal International*, 142(1), 151-161.
- 700 McBeck, J., Kobchenko, M., Hall, S. A., Tudisco, E., Cordonnier, B., Meakin, P., & Renard, F.,
701 (2018), Investigating the onset of strain localization within anisotropic shale using digital
702 volume correlation of time-resolved X-ray microtomography images. *Journal of*
703 *Geophysical Research: Solid Earth*, doi:10.1029/2018JB015676.
- 704 Mirone, A., Brun, E., Gouillart, E., Tafforeau, P., & Kieffer, J. (2014), The PyHST2 hybrid
705 distributed code for high speed tomographic reconstruction with iterative reconstruction
706 and a priori knowledge capabilities. *Nuclear Instruments and Methods in Physics*
707 *Research Section B: Beam Interactions with Materials and Atoms*, 324, 41-48.
708 doi:10.1016/j.nimb.2013.09.030.
- 709 Ngwenya, B. T., Main, I. G., Elphick, S. C., Crawford, B. R., & Smart, B. G. (2001), A
710 constitutive law for low-temperature creep of water-saturated sandstones. *Journal of*
711 *Geophysical Research: Solid Earth*, 106(B10), 21811-21826.
- 712 Peng, S., & Johnson, A. M. (1972), Crack growth and faulting in cylindrical specimens of
713 Chelmsford granite. *International Journal of Rock Mechanics and Mining Science*, 9, 37-
714 86.
- 715 Quintanilla-Terminel, A., & Evans, B. (2016), Heterogeneity of inelastic strain during creep of
716 Carrara marble: Microscale strain measurement technique. *Journal of Geophysical*
717 *Research: Solid Earth*, 121(8), 5736-5760.
- 718 Reches, Z., & Lockner, D. A. (1994), Nucleation and growth of faults in brittle rocks, *Journal of*
719 *Geophysical Research*, 99, 18159-18173.
- 720 Renard, F., Cordonnier, B., Dysthe, D. K., Boller, E., Tafforeau, P., & Rack, A. (2016), A
721 deformation rig for synchrotron microtomography studies of geomaterials under
722 conditions down to 10 km depth in the Earth. *Journal of Synchrotron Radiation*, 23(4),
723 1030-1034.

- 724 Renard, F., Cordonnier, B., Kobchenko, M., Kandula, N., Weiss, J., & Zhu, W. (2017),
 725 Microscale characterization of rupture nucleation unravels precursors to faulting in rocks.
 726 *Earth and Planetary Science Letters*, 476, 69-78.
- 727 Renard, F., McBeck, J., Kandula, N., Cordonnier, B., Meakin, P., & Ben-Zion, Y. (2019),
 728 Volumetric and shear processes in crystalline rock approaching faulting, *Proceedings of*
 729 *the National Academy of Sciences*, 116, 16234-16239, doi: 10.1073/pnas.1902994116.
- 730 Ross, J. V., Bauer, S. J., & Carter, N. L. (1983), Effect of the α - β quartz transition on the creep
 731 properties of quartzite and granite. *Geophysical Research Letters*, 10(12), 1129-1132.
- 732 Røyne, A., Bisschop, J., & Dysthe, D. K. (2011), Experimental investigation of surface energy
 733 and subcritical crack growth in calcite, *Journal of Geophysical Research*, 116, B04204,
 734 doi:10.1029/2010JB008033.
- 735 Rutter, E. H. (1976), A discussion on natural strain and geological structure-the kinetics of rock
 736 deformation by pressure solution. *Philosophical Transactions of the Royal Society of*
 737 *London. Series A, Mathematical and Physical Sciences*, 283(1312), 203-219.
- 738 Satoh, T., Shivakumar, K., Nishizawa, O., & Kusunose, K. (1996), Precursory localization and
 739 development of microfractures along the ultimate fracture plane in amphibolite under
 740 triaxial creep. *Geophysical Research Letters*, 23(8), 865-868.
- 741 Scholz, C. H. (1968), Mechanism of creep in brittle rock. *Journal of Geophysical Research*,
 742 73(10), 3295-3302.
- 743 Segall, P., & Pollard, D. D. (1980), Mechanics of discontinuous faults. *Journal of Geophysical*
 744 *Research: Solid Earth*, 85(B8), 4337-4350.
- 745 Shengqi, Y., & Jiang, Y. (2010), Triaxial mechanical creep behavior of sandstone. *Mining*
 746 *Science and Technology*, 20(3), 339-349.
- 747 Tal, Y., Evans, B., & Mok, U. (2016), Direct observations of damage during unconfined brittle
 748 failure of Carrara marble. *Journal of Geophysical Research: Solid Earth*, 121(3), 1584-
 749 1609.
- 750 Tsai, L. S., Hsieh, Y. M., Weng, M. C., Huang, T. H., & Jeng, F. S. (2008), Time-dependent
 751 deformation behaviors of weak sandstones. *International Journal of Rock Mechanics and*
 752 *Mining Sciences*, 45(2), 144-154.
- 753 Tudisco, E., Andò, E., Cailletaud, R., & Hall, S. A. (2017), TomoWarp2: a local digital volume
 754 correlation code. *SoftwareX*, 6, 267-270.
- 755 Vermilye, J. M., & Scholz, C. H. (1999), Fault propagation and segmentation: insight from the
 756 microstructural examination of a small fault. *Journal of Structural Geology*, 21(11),
 757 1623-1636.
- 758 Voight, B. (1989), A relation to describe rate-dependent material failure. *Science*, 243, 200-203.
- 759 Wei, S., Avouac, J. P., Hudnut, K. W., Donnellan, A., Parker, J. W., Graves, R. W., Helmberger,
 760 D., Fielding, E., Liu, Z., Cappa, F., & Eneva, M. (2015), The 2012 Brawley swarm
 761 triggered by injection-induced aseismic slip. *Earth and Planetary Science Letters*, 422,
 762 115-125.

- 763 Xu, S., & Ben-Zion, Y. (2013), Numerical and theoretical analyses of in-plane dynamic rupture
764 on a frictional interface and off-fault yielding patterns at different scales. *Geophysical*
765 *Journal International*, 193(1), 304-320.
- 766 Yang, S. Q., Xu, P., Ranjith, P. G., Chen, G. F., & Jing, H. W. (2015), Evaluation of creep
767 mechanical behavior of deep-buried marble under triaxial cyclic loading. *Arabian*
768 *Journal of Geosciences*, 8(9), 6567-6582.
- 769 Zhao, Q., Tisato, N., Kovaleva, O. & Grasselli, G. (2018), Direct observation of faulting by
770 means of rotary shear tests under X-ray micro-computed tomography. *Journal of*
771 *Geophysical Research*, 123 (9), 7389-7403.

Figure 1.

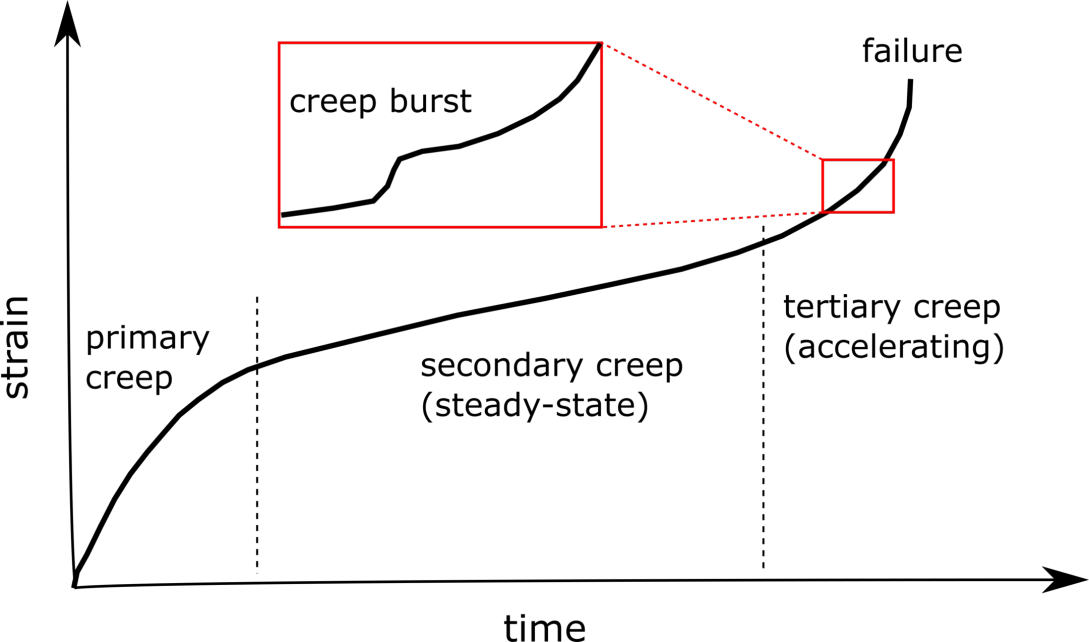
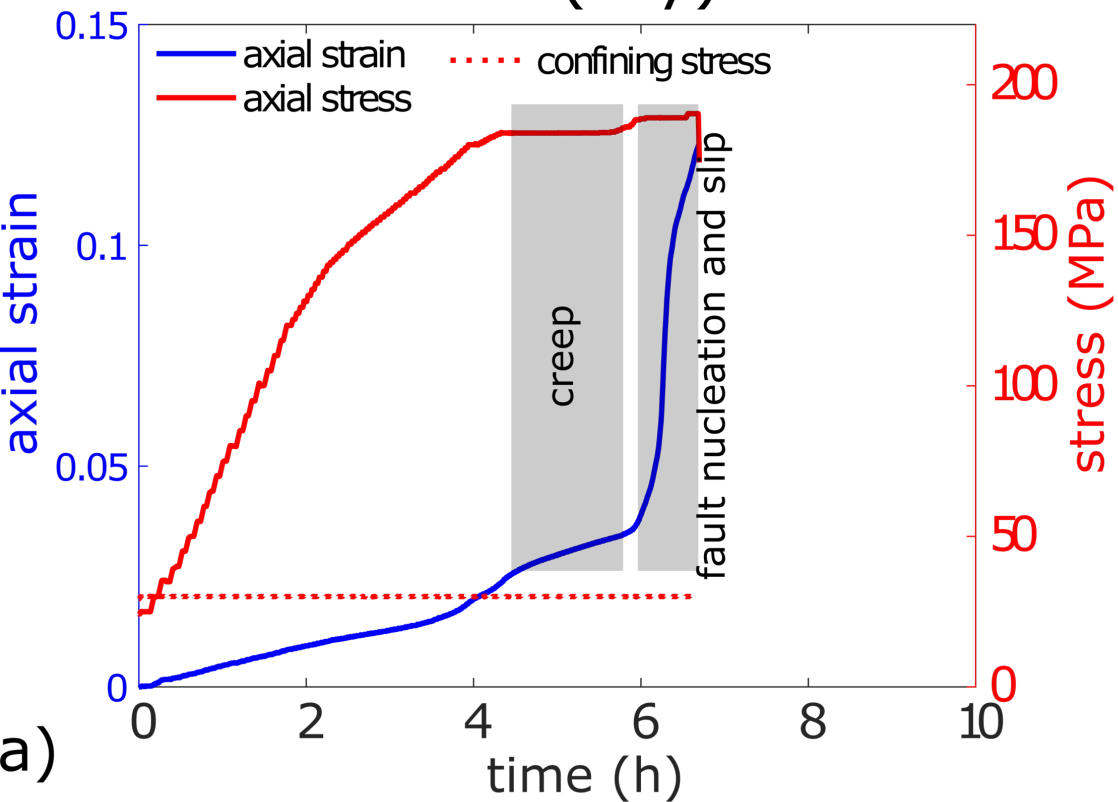


Figure 2.

M83 (dry)



M84 (wet)

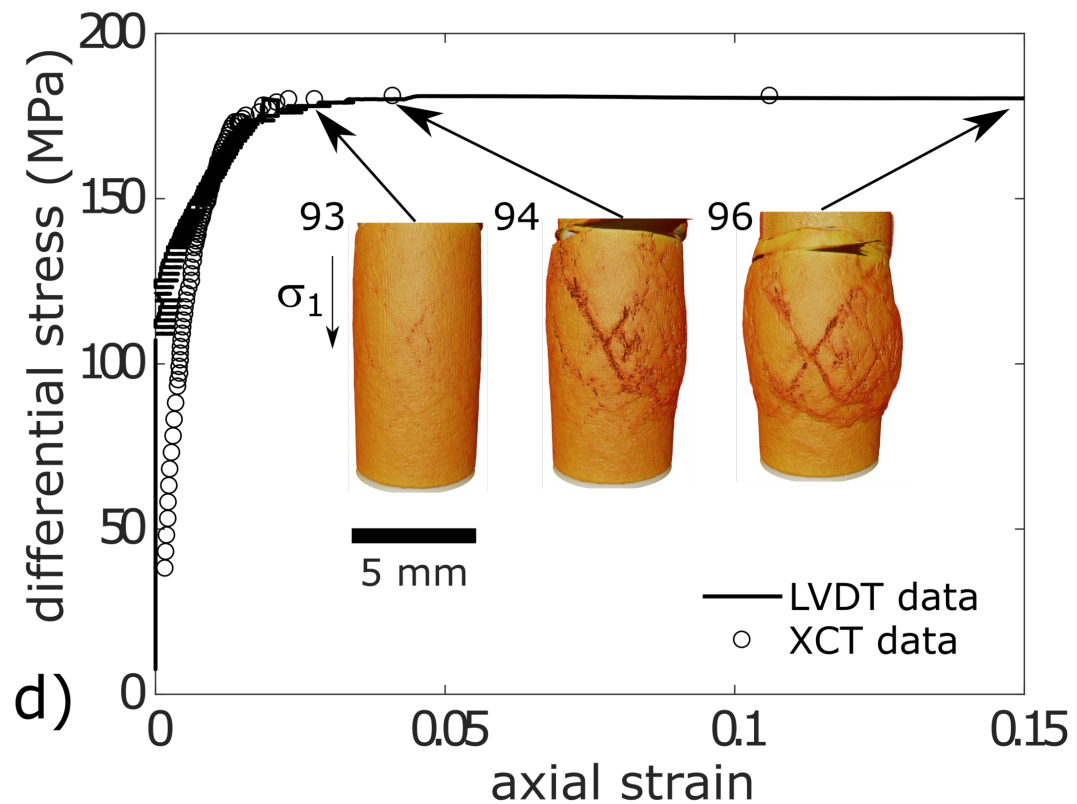
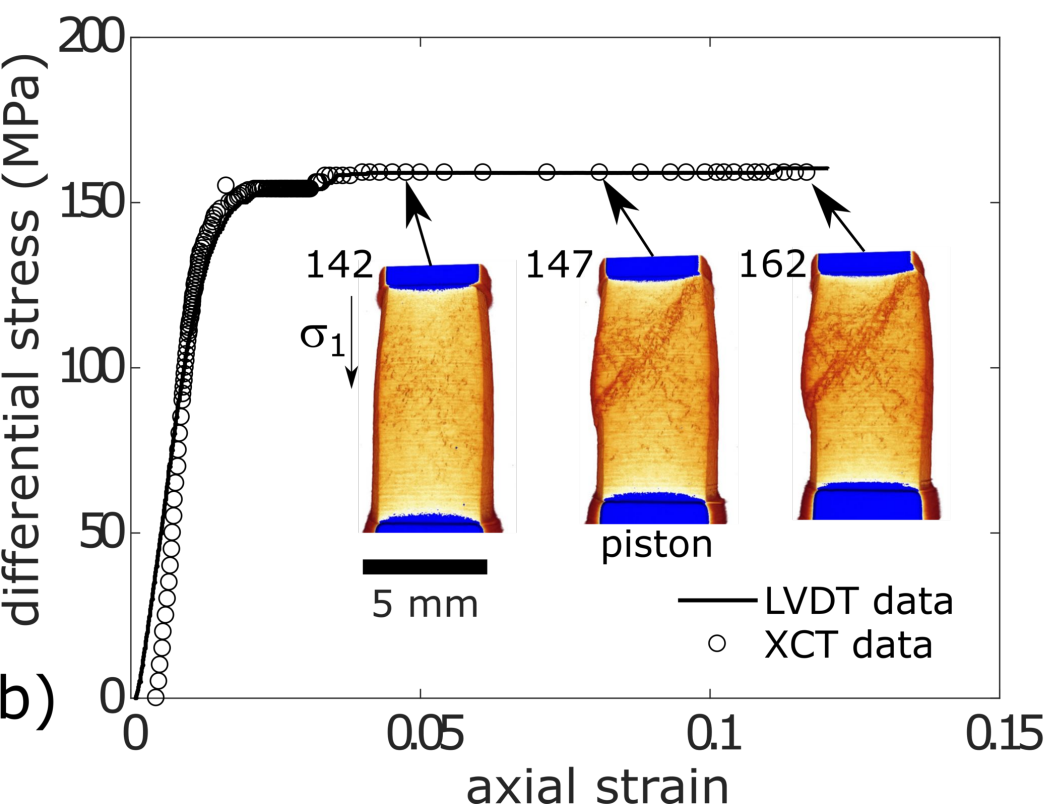
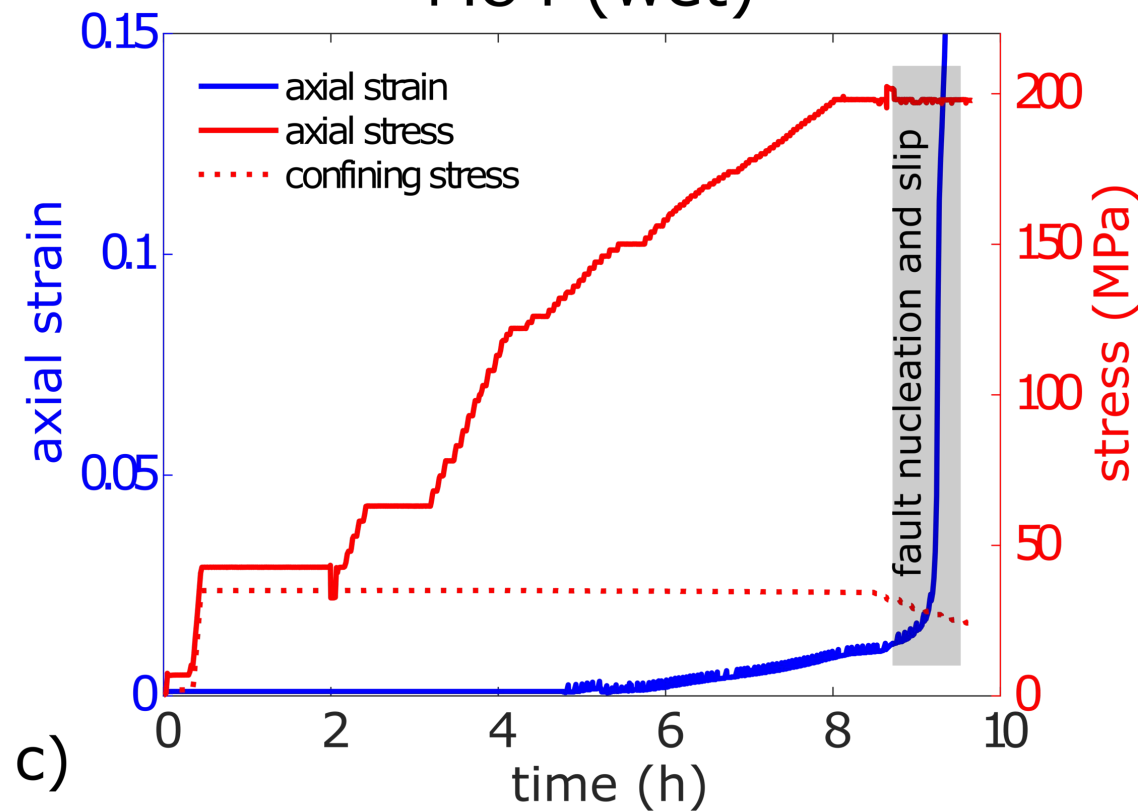


Figure 3.

Figure 4.

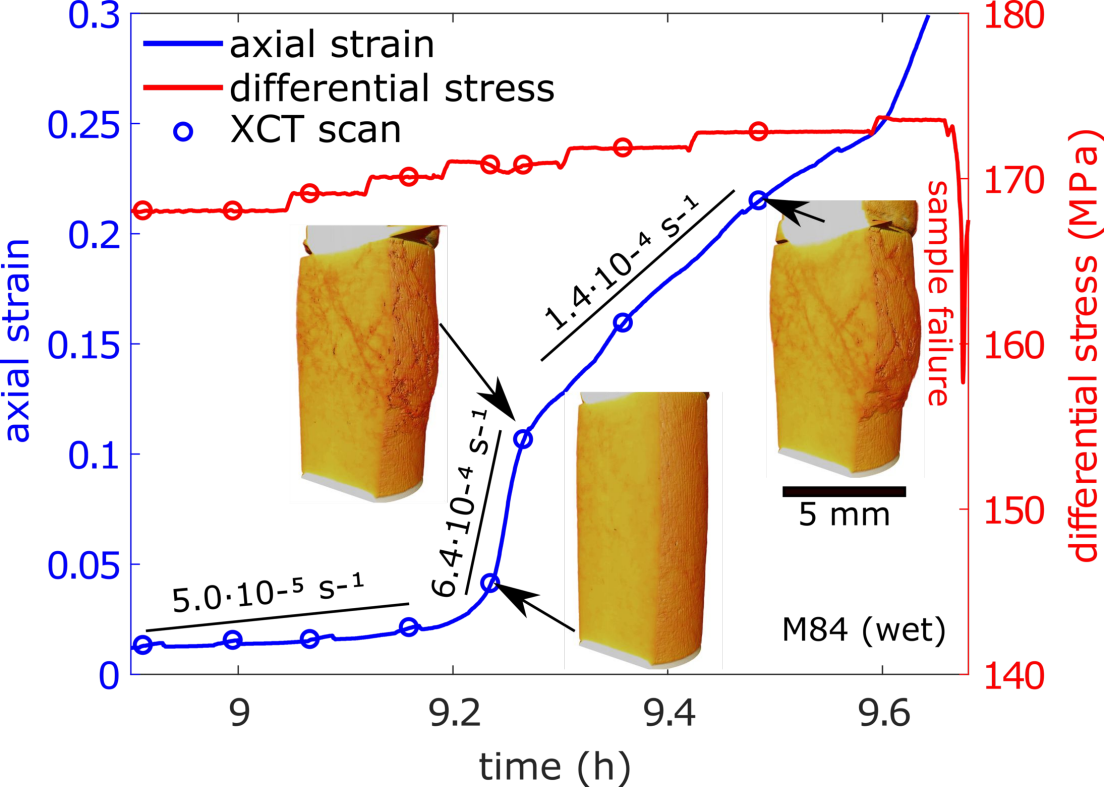


Figure 5.

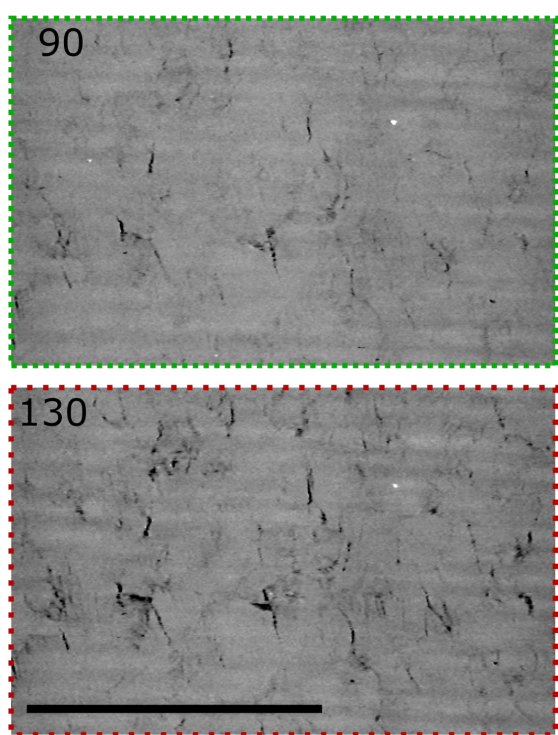
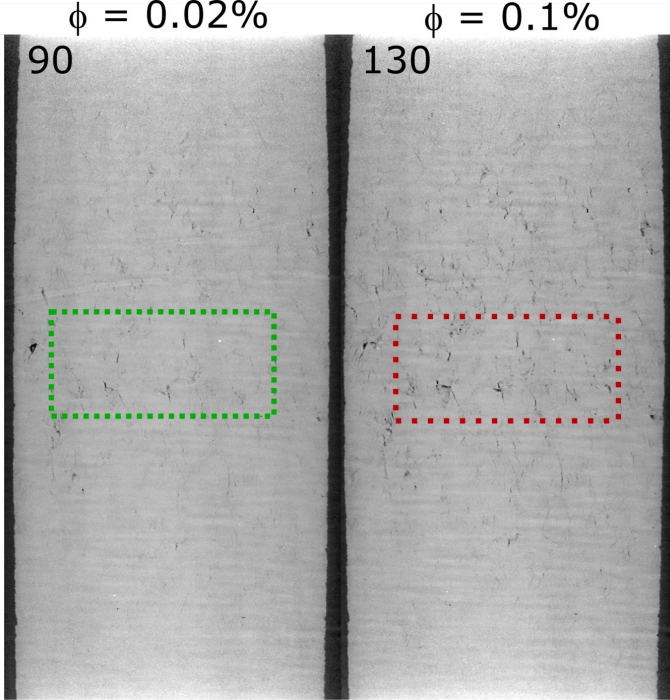


Figure 6.

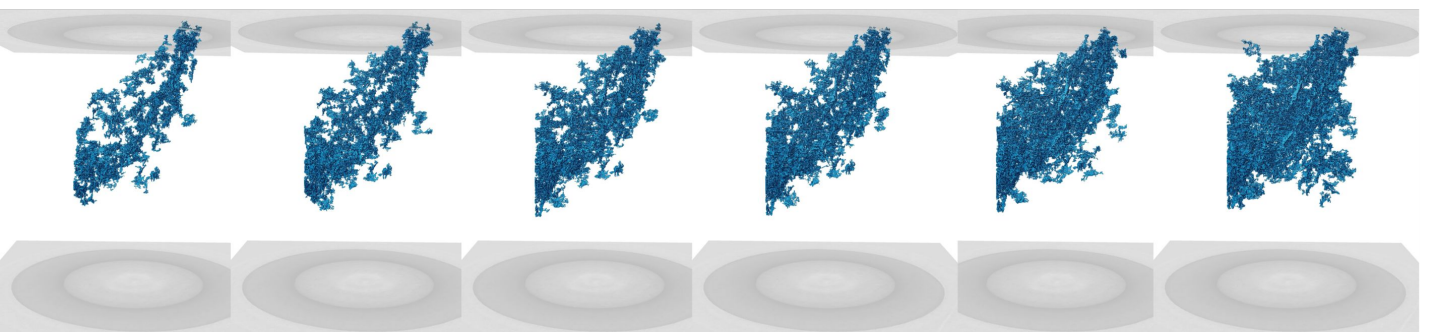
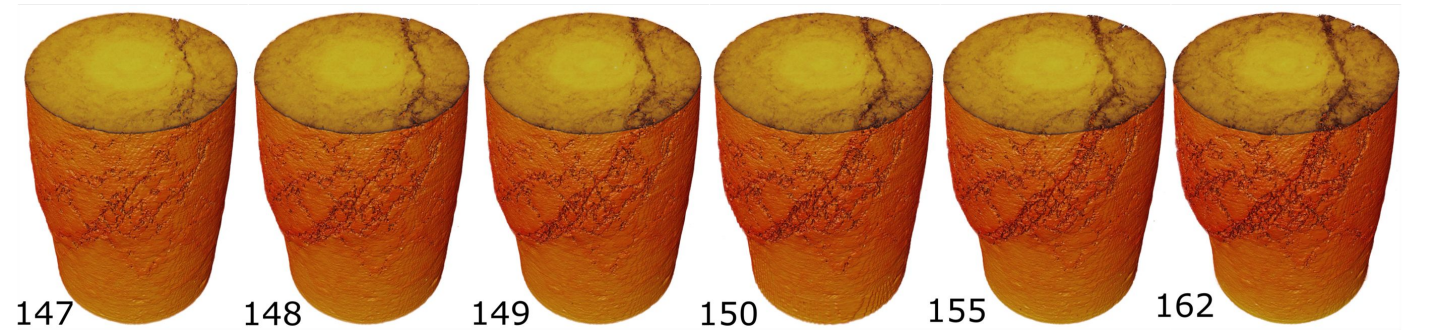
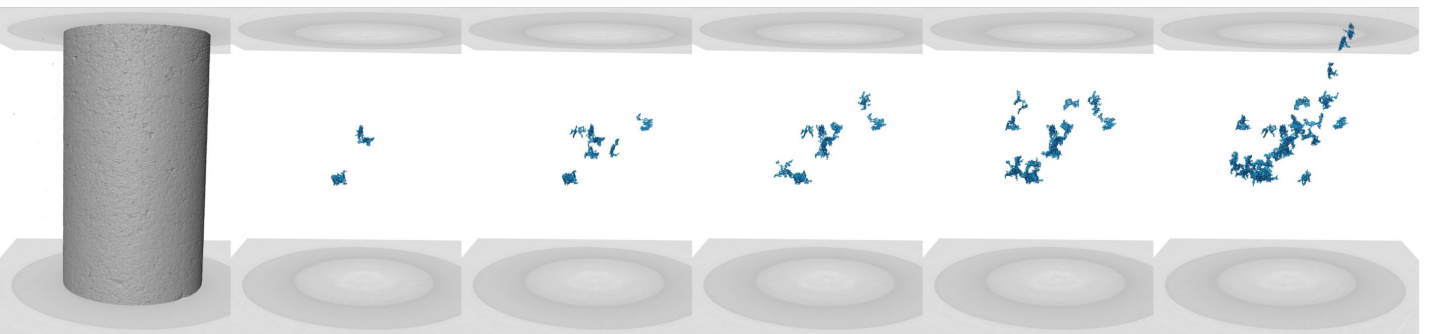
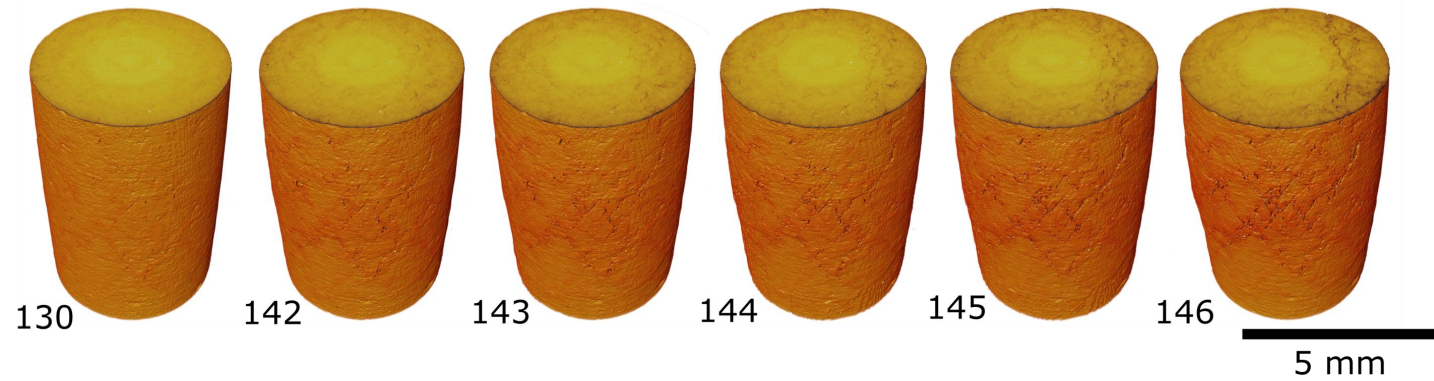


Figure 7.

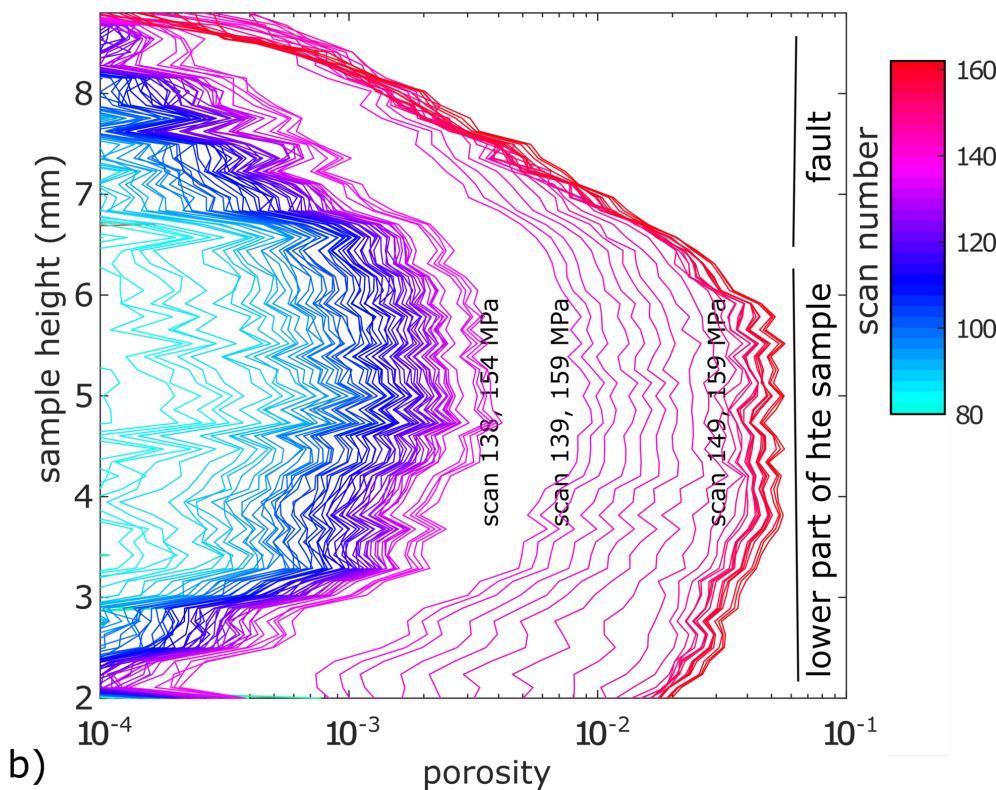
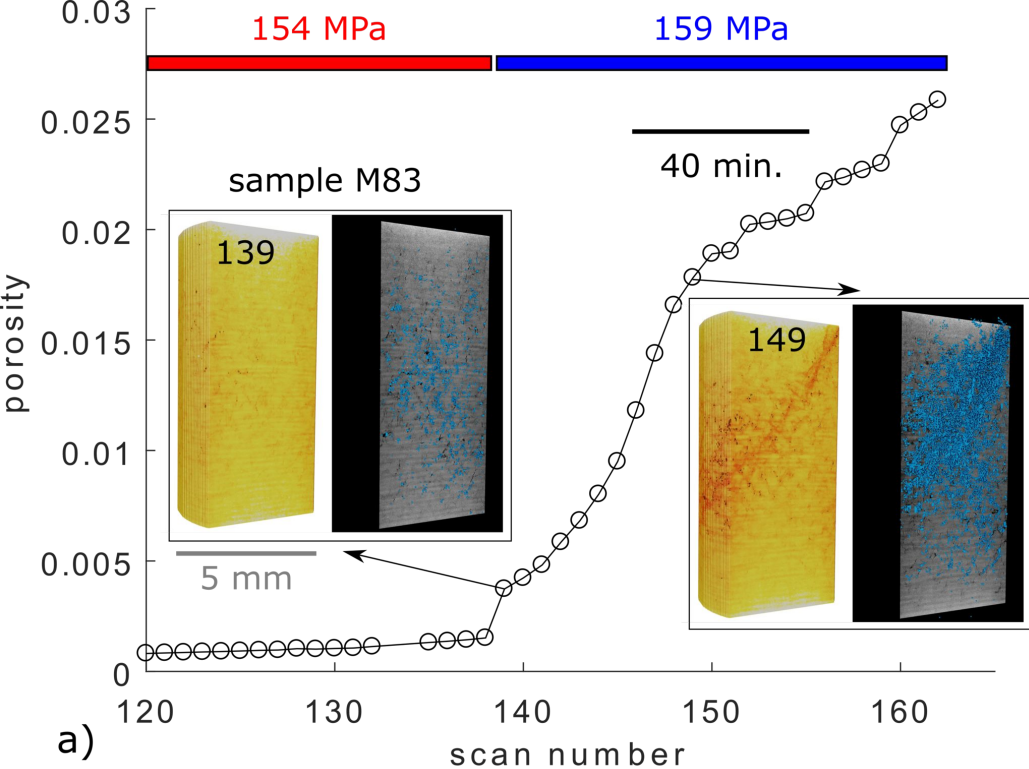
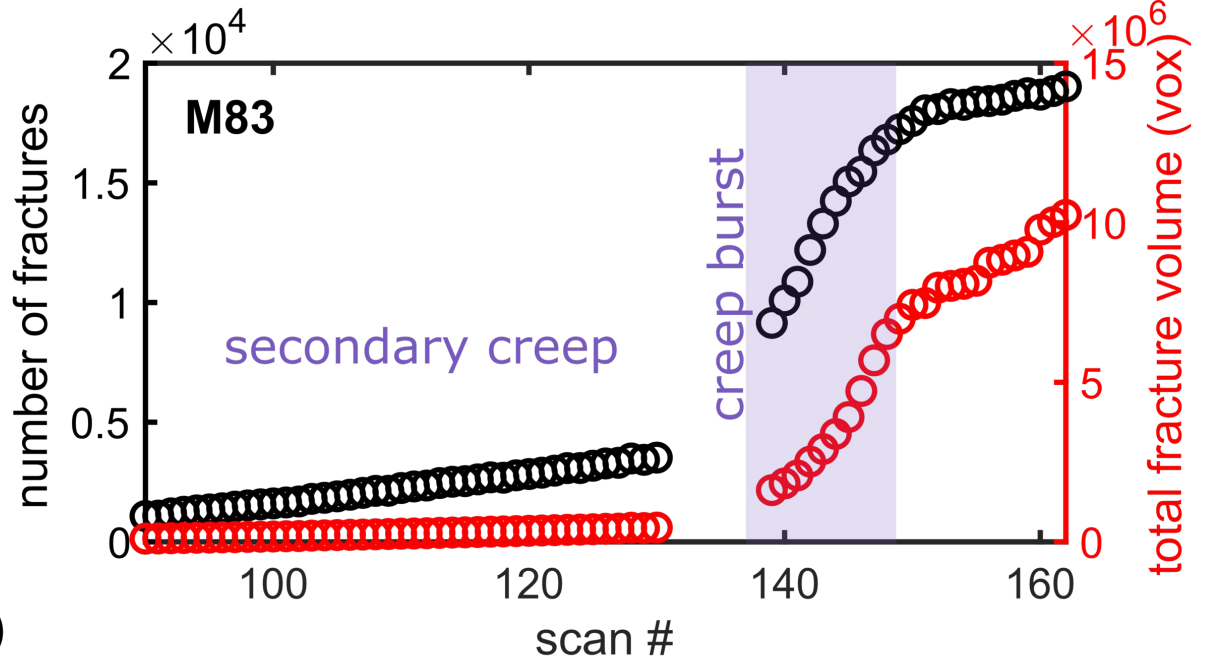
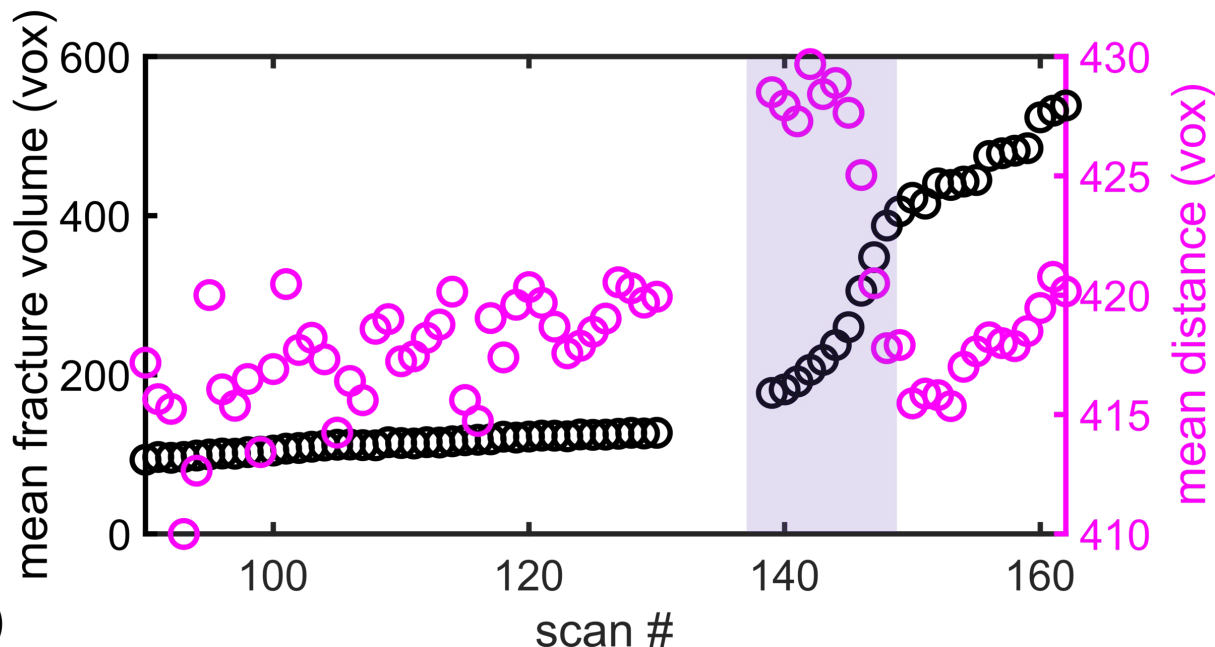


Figure 8.



a)



b)

Figure 9.

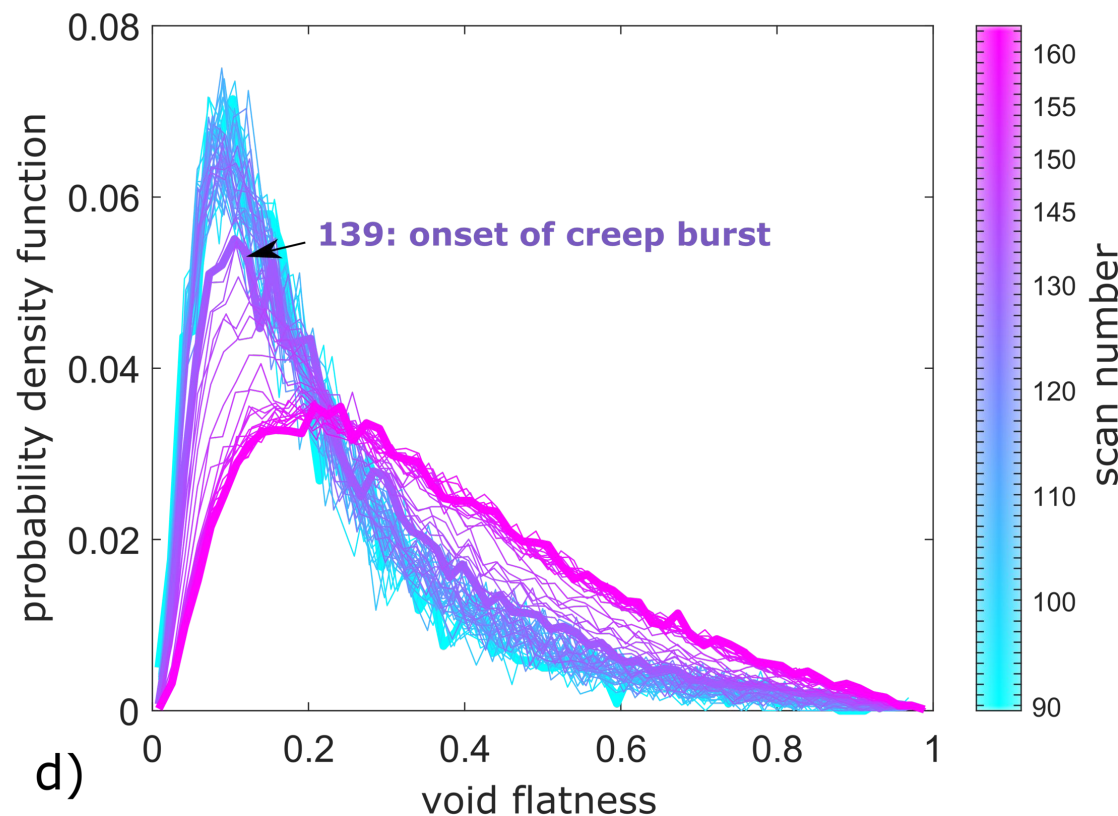
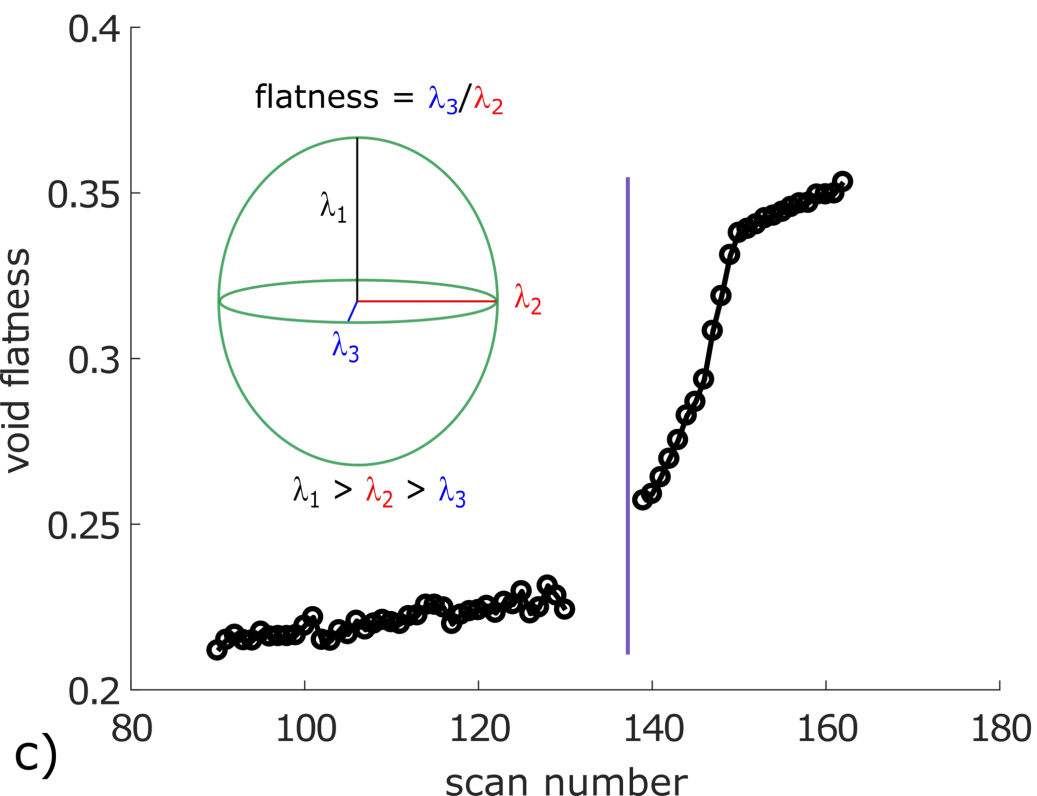
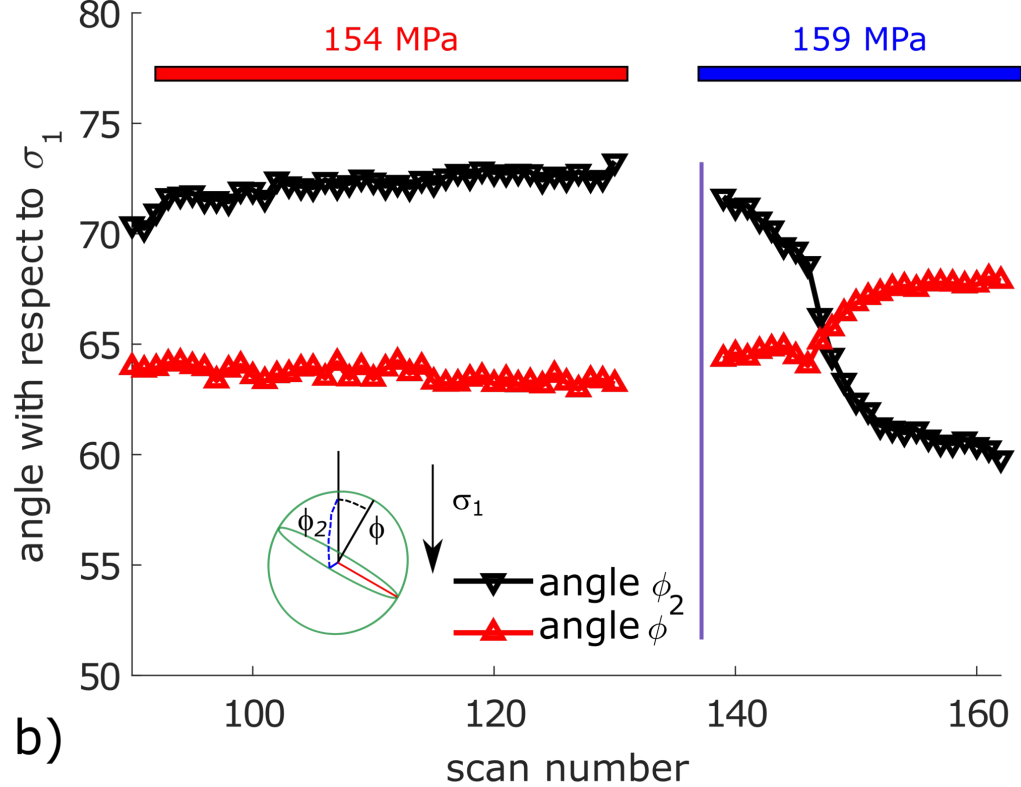
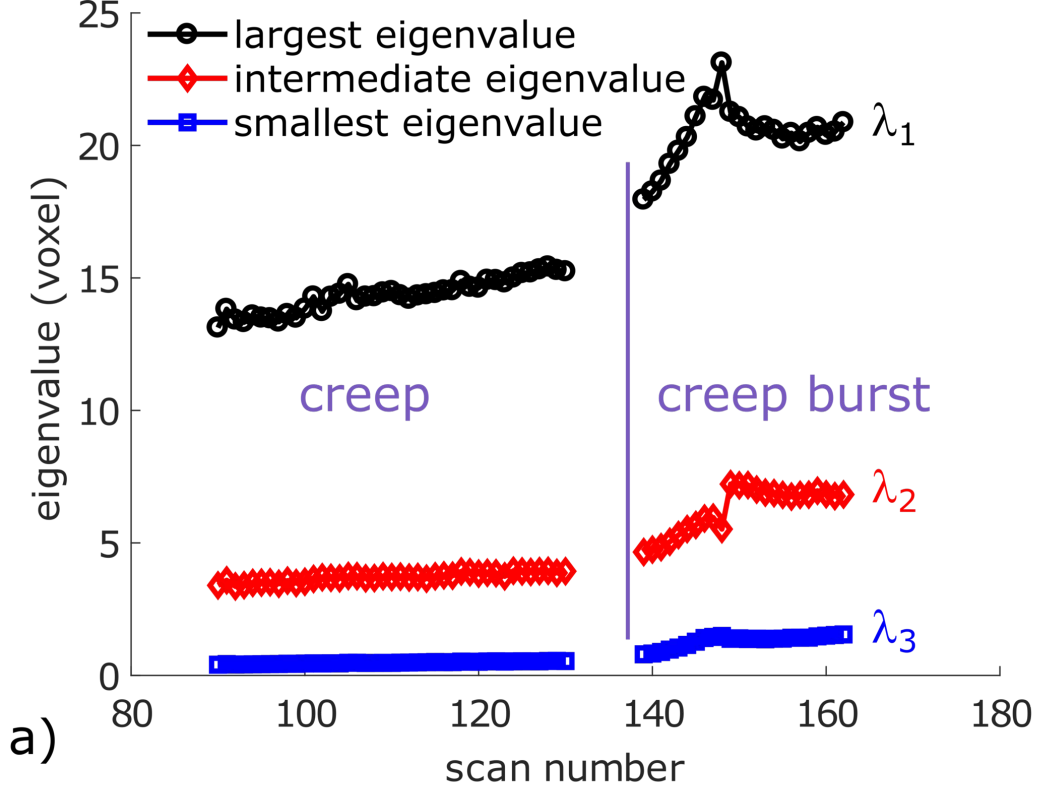


Figure 10.

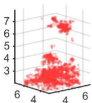
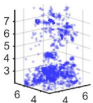
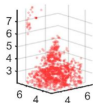
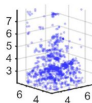
90-110

139-141

dilation

shear

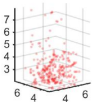
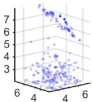
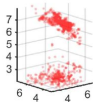
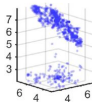
z (mm)



a) volumetric creep and fault nucleation

143-145

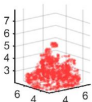
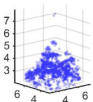
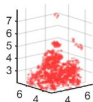
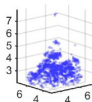
146-147



b) fault growth

152-154

158-160



c) fault locking and volumetric creep

Figure 11.

